Infrared radiation feedback does not regulate star cluster formation

Shyam H. Menon [1]★ Christoph Federrath [1,2] and Mark R. Krumholz [1,2]

[1]*Research School of Astronomy and Astrophysics, Australian National University, Canberra, ACT 2611, Australia*
[2]*ARC Centre of Excellence for Astronomy in Three Dimensions (ASTRO-3D), Canberra, ACT 2611, Australia*

ABSTRACT

We present 3D radiation-hydrodynamical (RHD) simulations of star cluster formation and evolution in massive, self-gravitating clouds, whose dust columns are optically thick to infrared (IR) photons. We use VETTAM – a recently developed, novel RHD algorithm, which uses the Variable Eddington Tensor closure – to model the IR radiation transport through the cloud. We also use realistic temperature (T) dependent IR opacities (κ) in our simulations, improving upon earlier works in this area, which used either constant IR opacities or simplified power laws ($\kappa \propto T^2$). We investigate the impact of the radiation pressure of these IR photons on the star formation efficiency of the cloud, and its potential to drive dusty winds. We find that IR radiation pressure is unable to regulate star formation or prevent accretion on to the star clusters, even for very high gas surface densities ($\Sigma > 10^5 \, \mathrm{M_\odot \, pc^{-2}}$), contrary to recent semi-analytic predictions and simulation results using simplified treatments of the dust opacity. We find that the commonly adopted simplifications of $\kappa \propto T^2$ or constant κ for the IR dust opacities leads to this discrepancy, as those approximations overestimate the radiation force. By contrast, with realistic opacities that take into account the microphysics of the dust, we find that the impact of IR radiation pressure on star formation is very mild, even at significantly high dust-to-gas ratios ($\sim$3 times solar), suggesting that it is unlikely to be an important feedback mechanism in controlling star formation in the ISM.

Key words: radiative transfer – methods: numerical – stars: formation – ISM: clouds – H II regions.

1 INTRODUCTION

Star formation is an inefficient process, as evidenced by observed gas depletion times,[1] which are two orders of magnitude above the dynamical time, both in galaxies (e.g. Leroy et al. 2017; Utomo et al. 2018), and in individual giant molecular clouds (GMCs) (e.g. Krumholz & Tan 2007; Evans, Heiderman & Vutisalchavakul 2014; Heyer et al. 2016; Pokhrel et al. 2020; Hu et al. 2022). Theoretical models explain this inefficiency through a combination of mechanisms that provide support against gravitational collapse, including turbulence, magnetic fields, stellar feedback, and dynamical stabilization (Krumholz & McKee 2005; Ostriker, McKee & Leroy 2010; Federrath & Klessen 2012; Krumholz, Klein & McKee 2012b; Federrath 2013b; Padoan et al. 2014; Federrath 2015; Burkhart 2018; Meidt et al. 2018; Krumholz & Federrath 2019; Evans, Kim & Ostriker 2022). Recent progress in both theory and observations have highlighted the pivotal role that feedback, especially due to massive (main-sequence) stars, plays in star/star-cluster formation (Krumholz et al. 2014; Krumholz, McKee & Bland-Hawthorn 2019), and the lifecycle of GMCs (see Chevance et al. 2020, 2022a for reviews). This massive-star feedback has been suggested to be largely responsible for limiting the integrated star formation efficiency (ϵ_*) to low values

in typical environments, where ϵ_* is given by

$$\epsilon_* = \frac{M_*}{M_{\mathrm{gas}}}, \tag{1}$$

which quantifies the net efficiency of star formation over the lifetime of a GMC, i.e. the ratio of the final stellar mass M_* and the available gas mass in the parent molecular cloud M_{gas}. Feedback achieves this by (i) disrupting GMCs in order $\sim$ unity dynamical time-scales, through the momentum and energy carried by feedback processes (e.g. Grudić et al. 2018), and (ii) driving turbulent motions that could further provide support against collapse (e.g. Mac Low & Klessen 2004; Krumholz, Matzner & McKee 2006; Elmegreen 2009; Gritschneder et al. 2009; Federrath et al. 2010; Wibking, Thompson & Krumholz 2018; Gallegos-Garcia et al. 2020; Menon, Federrath & Kuiper 2020; Menon et al. 2021).

Feedback from massive stars takes a number of forms: (i) the ionization of gas by the absorption of extreme ultraviolet (EUV) photons with energies that exceed their ionization potential (e.g. Dale, Ercolano & Bonnell 2012; Geen et al. 2016; Gavagnin et al. 2017; Kim, Kim & Ostriker 2018) (ii) radiation pressure on dust grains by the absorption of UV and IR photons (e.g. Krumholz & Matzner 2009; Fall, Krumholz & Matzner 2010; Murray, Quataert & Thompson 2010; Raskutti, Ostriker & Skinner 2016; Thompson & Krumholz 2016) (iii) winds driven by hot stars (e.g. Castor, Mc-Cray & Weaver 1975; Weaver et al. 1977; Lancaster et al. 2021a), and supernovae (SNe; Rogers & Pittard 2013; Calura et al. 2015). The first two of these are generally thought to be the most important. SNe, although important for driving turbulence in the diffuse ISM (e.g.

★ E-mail: shyam.menon@anu.edu.au

[1]The time-scale required by a galaxy, or a part thereof, to consume 100 per cent of its molecular gas supply at its current star formation rate.

Padoan et al. 2016) and controlling the dynamical state of gas at kpc scales (Kim & Ostriker 2017), are limited in their ability to control ϵ_* in GMCs due to the time delay of ~ 3 Myr between the onset of star formation and the first SNe – a time-scale within which either other 'early' feedback mechanisms disrupt the cloud, or a large fraction of gas converts to stars before feedback has a chance to stop it (Fall et al. 2010; Geen et al. 2016; Grudić et al. 2022). Indeed, observations confirm that most GMC disruption happens before SNe begin (e.g. Hollyhead et al. 2015; Grasha et al. 2019; Chevance et al. 2022b). Stellar winds have also shown to be inefficient at regulating ϵ_* due to a leakage of hot gas through low-density channels, and/or energy losses due to turbulent mixing at the hot-cool interface (Rogers & Pittard 2013; Rosen et al. 2014; Lancaster et al. 2021a). Among the former two mechanisms, photoionization has been understood to be the primary agent in regulating ϵ_* in environments with escape speeds lower than the sound speed of ionized gas (~ 10 km s^{-1}), whereas radiation pressure becomes dominant for denser environments that are beyond this limit (Krumholz & Matzner 2009; Murray et al. 2010; Kim et al. 2018; Fukushima & Yajima 2021). Such environments have been observed to exist at the formation sites of massive clusters, and/or for younger/compact systems (Lopez et al. 2011, 2014; Barnes et al. 2020; Olivier et al. 2021).

An additional source of radiation pressure can arise in high (surface) density environments that are optically thick to the dust-reprocessed IR photons, thereby undergoing repeated cycles of absorption and emission, enhancing the imparted momentum over the stellar UV photon momentum (Thompson, Quataert & Murray 2005; Murray et al. 2010). This is the so-called multiple-scattering regime, to differentiate it from the single-scattering regime, where the dust is optically thin to IR photons, and only the stellar photons can contribute. The enhancement in momentum imparted can be quantified by the trapping factor $f_{\rm trap} = \dot{p}_{\rm IR}/(L_*/c)$, where $\dot{p}_{\rm IR}$ is the momentum imparted per unit time integrated over all of a cloud by the IR photons, and L_*/c is the momentum per unit time carried by the direct stellar radiation field, which is also the momentum per unit time deposited in the gas in the single-scattering regime. Environments in the multiple-scattering regime in the local Universe are primarily found in extreme regions such as dwarf starbursts and ultraluminous infrared galaxies (ULIRGs) like Arp 220. These environments potentially host the formation sites of superstar clusters (SSC's; e.g. McCrady, Graham & Vacca 2005; Portegies Zwart, McMillan & Gieles 2010; Turner et al. 2015; Smith et al. 2020), and represent a dense mode of star formation that might have existed more commonly at high redshift. Observationally probing the natal phase of star formation in these environments is difficult due to the highly embedded nature of young forming SSCs. However, recent efforts using the Atacama Large Millimeter/Submillimeter Array (ALMA) have managed to do so at relatively high resolution (~ 2 pc; e.g. Turner et al. 2017; Leroy et al. 2018; Rico-Villas et al. 2020), with future instruments such as the *James Webb Space Telescope* (*JWST*) expected to enable further study. It is therefore of interest to develop theoretical models and conduct numerical simulations to determine the effectiveness of feedback in such environments and its subsequent influence on the efficiency of star formation.

The dynamical competition between gravity and (IR) radiation pressure has previously been studied through semi-analytical models and numerical simulations. For instance, Murray et al. (2010) built semi-analytic models, and found that IR radiation pressure is the dominant feedback mechanism in regulating ϵ_* in high-density environments. However, the findings of those studies were put into question by radiation–hydrodynamic (RHD) simulations of atmospheres in a gravitational field exposed to IR photon fluxes; these

simulations found that semi-analytic models overestimate the amount of momentum that is imparted, as they cannot capture the complex interactions between radiation and matter in higher dimensional, non-trivial (e.g. turbulent) density distributions (Krumholz & Thompson 2012, 2013; Davis et al. 2014; Rosdahl & Teyssier 2015; Tsang & Milosavljević 2015). However, these simulations were also highly idealized, with plane-parallel geometries, and static, fixed radiation fluxes and gravitational potentials. They also use an approximation for the IR opacities that we will show in this study, can significantly overestimate the effectiveness of the feedback. In the *direct* context of star cluster formation in turbulent, self-gravitating GMCs, Skinner & Ostriker 2015 (SO15 hereafter) performed the first systematic study with 3D RHD simulations. They found that the dust IR opacity (κ) is the most important parameter in determining ϵ_*: values of $\kappa \gtrsim 10$ cm^2 g^{-1} are required for having any regulatory effect on ϵ_*, which likely apply in dust-enriched environments. Tsang & Milosavljević (2018) reached similar conclusions using a more accurate RHD method, but only simulated one point in the parameter space explored in SO15.

Although the results from these simulations are suggestive and provide intuition, they do not fully resolve the question of how radiation feedback regulates ϵ_* in different environments. This is primarily because these studies probe a relatively narrow range in parameter space, specifically in surface density Σ, which is expected to be the most important environmental parameter when it comes to determining the value of $f_{\rm trap}$, and thus the effectiveness of IR radiation feedback (Murray et al. 2010). Recent semi-analytic work by Crocker et al. (2018, C18 hereafter) suggests the existence of a critical surface density $\Sigma_{\rm crit}$, such that clouds with $\Sigma > \Sigma_{\rm crit}$ may be unstable to the driving of winds by radiation pressure, effectively regulating ϵ_*. C18's proposed surface density threshold is

$$\Sigma_{\rm crit} \simeq 1.3 \times 10^5 \, {\rm M_\odot \, pc^{-2}} \left(\frac{Z}{Z_\odot} \right)^{-1} \left(\frac{\Psi(Z)}{\Psi_\odot} \right)^{-1}, \qquad (2)$$

where Z is the gas metallicity, Ψ is the light to mass ratio of the stellar population, and the subscript $\odot$ indicates values evaluated at Solar metallicity. The value of $\Sigma_{\rm crit}$ is comparable to the observed surface densities of the densest star clusters, but is larger than the highest Σ explored in simulations thus far by about 2 orders of magnitude. Another important caveat of the study is the use of idealized, spatially and temporally constant opacities, while the true opacity is dependent on the (local) dust and radiation temperatures. The temperature dependence of the opacity has been argued by C18 to be instrumental in giving rise to a critical surface density. In addition, it is the temperature dependence of opacities that produces subtle interactions of radiation and matter that govern the evolution of such systems (Krumholz & Thompson 2012).

Another limitation of SO15 is associated with the Moment-1 (M_1) approximation for RHD that is used in their simulations, which is known to produce incorrect radiation field distributions with multiple/extended sources (see for instance fig. 13 in Menon et al. 2022). In addition, the M_1 approach has been shown to underestimate the effective radiation forces, and to produce qualitatively different outcomes than are obtained with more accurate methods such as the Variable Eddington Tensor closure (VET; Davis et al. 2014; Zhang & Davis 2017) or direct solutions of the radiative transfer equation (Jiang 2021). Although Tsang & Milosavljević (2018) use an implicit Monte Carlo RHD method in their study, which has been shown to be of comparable accuracy to VET (Tsang & Milosavljević 2015), the fact that this study examined only a single point in parameter space makes it hard to draw conclusions about whether the M_1 results are robust more generally.

In this study, we address these limitations of prior work by studying the role of radiation feedback in regulating star formation in turbulent, self-gravitating clouds with more realistic IR dust opacities, dependent on temperature and density (e.g. Semenov et al. 2003). We use the recently developed VETTAM (Menon et al. 2022) algorithm for our simulations, which uses a VET method for radiation transfer. We explore clouds with different Σ, both below and beyond Σ_{crit}, to test the existence of a critical surface density, and if so, constrain its value. We also test environments that might be dust-enriched, to see what role this might play in controlling ϵ_*. Our simulations help understand star cluster formation in extreme environments such as the SSC-forming clouds, which are present-day counterparts of the precursors of globular clusters (Adamo et al. 2020). They also shed light on the intricacies governing the competition of IR radiation pressure and gravity, which is relevant to other systems, such as the driving of dusty winds in starburst galaxies (e.g. Zhang 2018; Zhang et al. 2018) or AGN-driven outflows (Bieri et al. 2017; Costa et al. 2018).

The paper is organized as follows: In Section 2 we describe the equations solved in our simulations, the numerical prescriptions we use, and the initial conditions of our clouds. In Section 3 we present the results of our simulation suite, exploring the effects of different treatments of the opacity and different environmental conditions. In Section 4 we discuss the implications of our results, and in Section 5 we conclude with a brief summary.

2 METHODS

2.1 Equations solved

In this study, we run 3D RHD simulations of gas clouds on Cartesian grids with gravity, and sink particles (Federrath et al. 2010c) to represent unresolved stellar clusters as point masses. We solve the non-relativistic, grey, RHD equations in the mixed-frame formulation (Mihalas & Klein 1982), retaining terms that are of leading order in all limiting regimes of RHD (see e.g. Krumholz et al. 2007), given by

$$\frac{\partial \rho}{\partial t} + \nabla \cdot (\rho \mathbf{v}) = 0 \tag{3}$$

$$\frac{\partial (\rho \mathbf{v})}{\partial t} + \nabla \cdot (\rho \mathbf{v}\mathbf{v}) = -\nabla P - \rho \nabla \Phi + \boldsymbol{G} \tag{4}$$

$$\frac{\partial E_r}{\partial t} + \nabla \cdot \boldsymbol{F} = -cG^0 + \dot{j}_* \tag{5}$$

$$\frac{\partial \boldsymbol{F}}{\partial t} + \nabla \cdot (c^2 E_r \mathbf{T}) = -c^2 \boldsymbol{G} \tag{6}$$

$$P = c_s^2 \rho, \tag{7}$$

where

$$G^0 = \rho \kappa_P \left(E_r - a_R T^4 \right) + \rho \left(\kappa_R - 2\kappa_P \right) \frac{\mathbf{v} \cdot \boldsymbol{F}}{c^2}$$
$$+ \rho \left(\kappa_P - \kappa_R \right) \left[\frac{v^2}{c^2} E_r + \frac{\mathbf{v}\mathbf{v}}{c^2} : \mathbf{P}_r \right], \tag{8}$$

and

$$\boldsymbol{G} = \rho \kappa_R \frac{\boldsymbol{F}}{c} - \rho \kappa_R E_r \frac{\mathbf{v}}{c} \cdot (\mathbf{I} + \mathbf{T}), \tag{9}$$

are the time-like and space-like parts of the specific radiation four-force density for a direction-independent flux spectrum (Mihalas & Auer 2001) to leading order in all regimes. In the above equations ρ is the mass density, P the gas thermal pressure, $\mathbf{v}$ the gas velocity,

Φ the gravitational potential, T the gas temperature, $\mathbf{I}$ the identity matrix, and c the speed of light in vacuum. In the radiation moment equations (equations 5 and 6), E_r is the lab-frame radiation energy density, $\boldsymbol{F}$ the lab-frame radiation momentum density, $\mathbf{P}_r$ is the lab-frame radiation pressure tensor, and κ_P and κ_R are the Planck and Rosseland mean opacities. Note that we denote tensor contractions over a single index with dots (e.g. $\boldsymbol{a} \cdot \boldsymbol{b}$), tensor contractions over two indices by colons (e.g. $\mathbf{A}:\mathbf{B}$), and tensor products of vectors without an operator symbol (e.g. $\boldsymbol{ab}$).

The radiation closure relation is used to close the above system of equations, and is of the form

$$\mathbf{P}_r = \mathbf{T} E_r, \tag{10}$$

where $\mathbf{T}$ is the Eddington Tensor. We use an Eddington tensor directly calculated from angular quadratures of the frequency-averaged specific intensity $I_r(\hat{\boldsymbol{n}}_k)$, using the relations

$$E_r = \int_0^\infty \mathrm{d}\nu \int \mathrm{d}\Omega \, I_r(\hat{\boldsymbol{n}}_k, \nu)/c, \tag{11}$$

$$\mathbf{P}_r = \int_0^\infty \mathrm{d}\nu \int \mathrm{d}\Omega \, \hat{\boldsymbol{n}}_k \hat{\boldsymbol{n}}_k \, I_r(\hat{\boldsymbol{n}}_k, \nu)/c, \tag{12}$$

where I_r as a function of the spatial path-length s is calculated from a formal solution of the time-independent radiative transfer equation,

$$\frac{\partial I_r}{\partial s} = \rho \kappa (S - I_r), \tag{13}$$

where S is the source function, which, for the purposes of modelling the emission from dust grains, we set equal to the frequency-integrated Planck function, $B(T_d) = ca_R T_d^4/(4\pi)$, where a_R is the radiation constant and T_d is the temperature of the dust grains that the radiation field most strongly interacts. The expression in equation (13) neglects scattering, and assumes that the dust emits and absorbs radiation in the comoving frame with the same grey opacity $\kappa = \int_0^\infty \kappa(\nu_0)\mathrm{d}\nu_0$, where $\kappa(\nu_0)$ is the material opacity at frequency ν_0. In addition, we also ignore $\mathcal{O}(v/c)$ terms in this equation, which arise from the mixed-frame formulation, since we expect the contribution of these terms to the Eddington tensor to be relatively small. We also require a closure relation for the gas pressure P, the details of which we discuss in Section 2.2.2.

2.2 Numerical scheme

We solve the equations outlined in the previous section using the Variable Eddington Tensor-closed Transport on Adaptive Meshes (VETTAM; Menon et al. 2022) method, a state-of-the-art RHD algorithm integrated into a modified version of the FLASH magnetohydrodynamics code (Fryxell et al. 2000; Dubey, Reid & Fisher 2008). FLASH solves the hydrodynamic equations on an Eulerian mesh, with Adaptive Mesh Refinement (Berger & Colella 1989) using the PARAMESH library (MacNeice et al. 2000).

2.2.1 Hydrodynamics

The hydrodynamic updates are performed using pre-existing infrastructure available in FLASH. We use an explicit Godunov method in the split, five-wave HLL5R (approximate) Riemann solver (Waagan, Federrath & Klingenberg 2011). This solver uses a piecewise linear reconstruction of the conserved variables (i.e. second-order accuracy) in such a way to ensure positivity, and has been shown to be of comparable accuracy to the Roe Riemann solver, but more stable (Waagan et al. 2011).

2.2.2 Gas and dust temperatures

We assume an isothermal equation of state in our simulations, i.e. $P = c_s^2 \rho$, where c_s is the thermal sound speed of the gas. We do not expect this approximation to impact our results significantly as the thermal pressure would be subdominant over the radiation pressure in our simulations, and presumably plays a minor role in affecting the dynamics of our clouds.[2]

We now comment on our treatment of T_d in this study. Ideally, one would use a scheme where the gas, dust, and radiation temperatures are treated separately and consistently, obtained by solving the coupled equations of their respective heating and cooling mechanisms (e.g. Bate & Keto 2015). Instead, we invoke the condition of radiative equilibrium, i.e. that all radiation absorbed by dust is instantly re-emitted locally, and $T_d = T_r$, which, in effect, means setting the radiation-dust energy exchange term $\rho \kappa_P c(a_R T_d^4 - E_r)$ to zero. This is a very reasonable approximation; we refer the reader to Appendix A of Krumholz & Thompson (2013) where this is justified.

The approximations mentioned above, in effect, implies that the gas temperature is completely decoupled from T_d, and thus, T_r. However, this assumption fails at the higher densities we probe ($n > 10^4 - 10^5$ cm^{-3}), where dust and gas temperatures are expected to become coupled to each other by collisions, and this in turn couples the gas temperature to the radiation field (i.e. $T_d = T_g = T_r$). In this limit, T_g, and hence the associated thermal pressure P, would be affected by the distribution of T_r, and our isothermal approximation is not correct. However, this matters little for the purposes of this study since, as noted above, thermal pressure is not a significant force in the systems we are simulating, regardless of the value of T_g. The primary harm in using an incorrect gas pressure is that the fragmentation properties in our simulations are unreliable. However, as we discuss below, we lack the resolution to attempt to reproduce fragmentation into individual stars in any event. By contrast, properties like the star formation efficiency, and the radiation-gravity force balance – which comprise the focus of this paper – are unaffected.

2.2.3 Gravity and star formation

We use a multigrid algorithm implemented in FLASH (Ricker 2008) to solve the Poisson equation to obtain the gas gravitational potential. To follow the evolution of gas at unresolved scales, we use sink particles, formed when the local gas properties satisfy a set of conditions (see Federrath et al. 2010c), which we briefly describe here. Sink particles may form when the local gas density exceeds the Jeans threshold density $\rho_{\rm sink}$, given in terms of the Jeans length λ_J,

$$\rho_{\rm sink} = \frac{\pi c_s^2}{G \lambda_J^2}, \tag{14}$$

where c_s is the local sound speed, and G the gravitational constant. The Jeans length is linked to the accretion radius of the sink particle by $r_{\rm sink} = \lambda_J/2$. To avoid artificial fragmentation (Truelove et al. 1997), the sink particle diameter is set to $2r_{\rm sink} = 5\Delta x_{\rm min}$, where $\Delta x_{\rm min}$ is the cell size at the highest level of AMR. However, the condition that a local region exceeds the density threshold given by equation (14) is only a necessary, but not sufficient condition for sink particle formation. In addition, the algorithm checks that

all gas within the control volume with radius $r_{\rm sink}$ is gravitationally bound (taking into account thermal, kinetic, and magnetic energies), collapsing towards the centre of the control volume, and does not already contain a previously formed sink particle – only then is a sink particle formed. This procedure is crucial to avoid spurious formation of sink particles (Federrath et al. 2010c). Once created, a sink particle can accrete gas, if computational cells within $r_{\rm sink}$ exceed $\rho_{\rm sink}$, and satisfy the additional conditions above. During accretion, mass, momentum, and angular momentum are conserved. We compute the gravitational interaction of sink particles with the gas by direct summation over all sink particles and grid cells (Federrath et al. 2011a), and we use a second-order leapfrog integrator to advance the sink particle positions and velocities.

2.2.4 Radiation from sink particles

We include the direct contribution of radiation energy from sink particles, which, given that our resolution is insufficient to capture individual stars, represent unsolved ministar clusters. We determine sink particle luminosities by adopting a fixed light-to-mass ratio $\langle L_*/M_* \rangle = 1.7 \times 10^3$ erg s^{-1} g^{-1} appropriate for a young stellar population, so that a particle of mass M_* has luminosity $L_* = \langle L_*/M_* \rangle M_*$. We inject this radiant energy into the simulation by adding a source term $\dot{j}_*$ in equation (5). For simplicity, and to be consistent with earlier works, we model $\dot{j}_*$ as a Gaussian kernel of size σ_*, given by

$$j_*(r) = \frac{L_*}{\left(2\pi\sigma_*^2\right)^{3/2}} \exp\left(-\frac{r^2}{2\sigma_*^2}\right), \tag{15}$$

where r is the radial distance of a grid cell from the sink particle. We adopt a value of $\sigma_* = 2\Delta x_{\rm min}$, where $\Delta x_{\rm min}$ is the minimum cell size in the domain. We demonstrate that our results are fairly insensitive to this choice by comparing runs with different σ_* in Appendix A1. We note that this term is meant to represent the UV radiation that has been reprocessed into the IR by dust on subgrid scales that we do not resolve, and is somewhat idealized. A more accurate treatment would involve following the radiation field in both the UV and IR bands, and self-consistently capturing the reprocessing of UV to IR in the simulation domain. We intend to adopt this approach in future work.

2.2.5 Radiation transport

We operator-split the radiation moment equations from the hydrodynamic and gravity updates, and solve them using the VETTAM scheme described in Menon et al. (2022). We refer readers to that paper for a full description of the algorithm, and provide a brief summary here. VETTAM solves the radiation moment equations using a first-order Godunov method with a piece-wise constant reconstruction of the conserved variables, and an HLLE Riemann solver for the discretized divergence terms in the transport equation. It uses a first-order backward Euler temporal discretization to enable time-steps set by the hydrodynamic signal speed rather than the speed of light. VET-TAM solves the moment equations with a non-local, self-consistent, radiation closure relation (equation 10) obtained from a solution of the time-independent radiative transfer equation (equation 13) using a hybrid characteristics ray-tracing scheme (Buntemeyer et al. 2016). The closure relation is computed once at the start of the time-step, and kept fixed for the update in a given time-step. The discretization, along with the estimate of **T**, leads to a coupled global system of equations, which we express in a matrix form. We use sparse matrix

---

[2]It is possible that thermal pressure contributes to the dynamics at late times in some of our simulations, when radiation manages to push most of the gas in the cloud to the outskirts of the domain. However, at this point, most of the gas is already removed from the cloud by radiation pressure, and hence, thermal pressure does not play a significant role.

solvers based on Krylov subspace methods (Saad 2003) to invert the matrices and obtain the (approximate) solution. VETTAM uses the open-source PETSc library (Balay et al. 2021) for this purpose.

We note that the solution of the time-independent transfer equation obtained with our ray-tracer provides the equilibrium solution for the given gas distribution. This would represent the true solution for situations where the time-scale of radiation is short compared to dynamical time-scales. While this condition is largely satisfied, it is possible that for some of our simulations with high optical depths, the time-scale of radiation diffusion be comparable to dynamical time-scales, and therefore the solution of the radiation intensity with the ray-tracer may not be entirely accurate. However, since this is only used for calculating **T** – the radiation is still transported with a time-dependent moment method that retains the right signal speeds – we do not expect any significant impacts on our results.

2.3 Dust IR opacities

The IR dust opacity is central to the magnitude of the radiation force and thus the competition between radiation and gravity forces in this problem. We thus test three different (approximate) dust opacity laws in our study, which represent three different levels of accuracy. Since we neglect the gas-radiation energy exchange term, we take $\kappa_P = 0$, and the only grey opacity in the problem is the Rosseland opacity κ_R. First, we test the simple assumptions of a spatially and temporally constant grey opacity with value κ_c as a starting point, and to serve as a tool of comparison with other works that adopt this approximation (Skinner & Ostriker 2015; Tsang & Milosavljević 2018). However, this is not expected to be physically accurate, as the IR dust opacity is strongly dependent on the both the radiation colour temperature and the dust temperature – which are nearly identical in an optically thick environment such as the one we are simulating (see Section 2.1). As discussed earlier in Section 1, the temperature dependence of the IR opacities is important for force balance, an effect we intend to explore in this study.

Our second approach is therefore to run simulations with a temperature- (and density-) dependent Semenov et al. (2003) opacity law, based on the microphysical, optical properties of dust grains. We refer to the κ_R returned by the Semenov opacity model as $\kappa_{Sem} \equiv \kappa_{Sem}(\rho, T_r)$, based on a publicly available code[3] by Semenov et al. (2003). We use the model of 'normal' silicates (NRM) with a relative iron content in silicates of Fe/(Fe + Mg) = 0.3, and assume that dust grains can be modelled as composite aggregates. However, we demonstrate in Appendix A2 that adopting different dust models has a negligible effect on our results. We show example curves of κ_{Sem} versus T_r in Fig. 1. The discontinuous features in the curves of κ_{Sem} arise due to different chemical species in the dust sublimating at those temperatures (Semenov et al. 2003). The exact sublimation temperature of various species depends on the gas (or dust) density ρ, which leads to the subtle differences in the curves for different values of ρ near the discontinuities.[4]

---

[3]https://www2.mpia-hd.mpg.de/~semenov/Opacities/opacities.html

[4]There is a small subtlety here worth pointing out. The Semenov et al. (2003) model is derived under the assumption of full local thermodynamic equilibrium between dust, gas, and radiation, so a single temperature characterizes all three, but at lower densities we are in a regime where T_r and T_d are nearly equal, but T_g may be different. This raises the question of which temperature we should use when evaluating the Semenov et al. model opacity. We choose to use $T_r = T_d$, because this captures the two most important temperature-dependent effects: the change in quantum efficiency of grain absorption in response to the change in λ/a, where λ is the radiation wavelength and a is
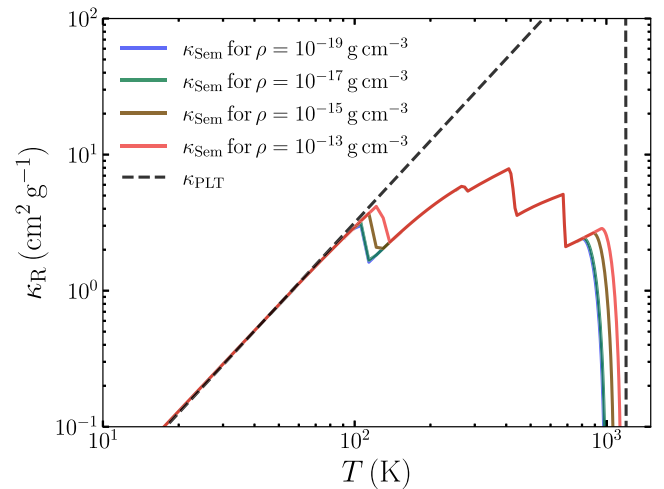

Figure 1. Plot showing $\kappa_{Sem}(\rho, T_r)$, the IR Rosseland opacities obtained with the Semenov et al. (2003) model as a function of radiation temperature (T_r) for various gas densities ρ (solid lines). The black dashed lines indicate κ_{PLT}, the IR opacities obtained with the power-law approximation given by equation (16). The sharp drop for this curve is associated with a floor of $\kappa_R = 10^{-3} \, \text{cm}^2 \, \text{g}^{-1}$ we set to emulate dust sublimation for $T > T_{sub}$, where $T_{sub} = 1200 \, \text{K}$ is the sublimation temperature of dust assumed.

Our third method of treating opacities is to explore simulations where we adopt a power-law dependence on the temperature for κ_R, which we refer to as κ_{PLT} given by

$$\kappa_{PLT}(T_r) = \begin{cases} 10^{-1.5} \, \text{cm}^2 \, \text{g}^{-1} \left(\frac{T_r}{10 \, \text{K}} \right)^2, & T_r < 1200 \, \text{K} \\ 10^{-3} \, \text{cm}^2 \, \text{g}^{-1}, & T_r \geq 1200 \, \text{K} \end{cases} . \quad (16)$$

This opacity law has been adopted in various studies that investigated balance of radiation and gravity forces in idealized experiments (e.g. Krumholz, Dekel & McKee 2012a; Krumholz & Thompson 2013; Davis et al. 2014), and is a central ingredient in the semi-analytical model of Crocker et al. (2018); note that the break at 1200 K in this model simply represents the temperature at which dust sublimes and the opacity drops to tiny values. While this approximation is in accord with the model of Semenov et al. (2003) at temperatures $\leq 150 \, \text{K}$, at higher temperatures, the values of κ_R are greatly overestimated. We demonstrate this by comparing κ_{PLT} as a function of T_r with κ_{Sem} in Fig. 1. Even at low values of $T_r \sim 300 \, \text{K}$, we see that κ_R is overestimated by a factor ~ 2, and this gets progressively worse at higher values of T_r.

2.4 Initial and boundary conditions

We now describe our initial and boundary conditions. We initialize our simulations as a uniform spherical cloud with mass (M_{cloud}) and radius R_{cloud}, which together define a cloud mass density $\rho_{cloud} = M_{cloud}/[(4/3)\pi R_{cloud}^3]$ and a mass surface density $\Sigma_{cloud} = M_{cloud}/(\pi R_{cloud}^2)$. We list the value of M_{cloud} and R_{cloud} for all our simulations in Table 1.

the grain size, and the sublimation of dust grains once their temperature rises too high. The main effect that our approximation misses is that changes in the rate of gaseous deposition on to grains (or spallation off grains) depends on the kinetic energy of gas molecules, and thus on T_g. However, this is a second-order effect compared to quantum efficiency and grain sublimation, so, in the absence of a more general grid of dust models that considers the case $T_g \neq T_d$, using $T_r = T_d$ in the Semenov et al. 2003 model is the best alternative.

Table 1. Main simulation parameters.

Model	M_{cloud} $(10^6\,\mathrm{M_\odot})$	R_{cloud} (pc)	Σ_{cloud} $(\mathrm{M_\odot\,pc^{-2}})$	n_{cloud} $(\mathrm{cm^{-3}})$	α_{vir}	σ_v $(\mathrm{km\,s^{-1}})$	$\mathcal{M}$	f_{DG}	κ_{R}
			κ_{c} Series: Section 3.1						
S3K01A2F1	1.0	10.0	3.2×10^3	9.7×10^3	2	23	11.5	1	$\kappa_{\mathrm{c}}=1\,\mathrm{cm^2\,g^{-1}}$
S3K05A2F1	1.0	10.0	3.2×10^3	9.7×10^3	2	23	11.5	1	$\kappa_{\mathrm{c}}=5\,\mathrm{cm^2\,g^{-1}}$
S3K10A2F1	1.0	10.0	3.2×10^3	9.7×10^3	2	23	11.5	1	$\kappa_{\mathrm{c}}=10\,\mathrm{cm^2\,g^{-1}}$
S3K20A2F1	1.0	10.0	3.2×10^3	9.7×10^3	2	23	11.5	1	$\kappa_{\mathrm{c}}=20\,\mathrm{cm^2\,g^{-1}}$
S3K40A2F1	1.0	10.0	3.2×10^3	9.7×10^3	2	23	11.5	1	$\kappa_{\mathrm{c}}=40\,\mathrm{cm^2\,g^{-1}}$
S3K80A2F1	1.0	10.0	3.2×10^3	9.7×10^3	2	23	11.5	1	$\kappa_{\mathrm{c}}=80\,\mathrm{cm^2\,g^{-1}}$
			Σ_{cloud} Series: Section 3.2						
S3KsemA2F1	1.0	10.0	3.2×10^3	9.7×10^3	2	23	11.5	1	κ_{Sem}
S4KsemA2F1	1.0	3.2	3.2×10^4	3.1×10^5	2	40	11.5	1	κ_{Sem}
S5KsemA2F1	1.0	1.0	3.2×10^5	9.7×10^6	2	72	11.5	1	κ_{Sem}
S6KsemA2F1	1.0	0.3	3.2×10^6	3.1×10^8	2	128	11.5	1	κ_{Sem}
			α_{vir} Series: Section 3.2.3						
S5KsemA3F1	1.0	1.0	3.2×10^5	9.7×10^6	3	88	11.5	1	κ_{Sem}
S5KsemA4F1	1.0	1.0	3.2×10^5	9.7×10^6	4	102	11.5	1	κ_{Sem}
			f_{dg} Series: Section 3.3						
S4KsemA2F2	1.0	3.2	3.2×10^4	3.1×10^5	2	40	11.5	2	κ_{Sem}
S4KsemA2F3	1.0	3.2	3.2×10^4	3.1×10^5	2	40	11.5	3	κ_{Sem}
S5KsemA2F2	1.0	1.0	3.2×10^5	9.7×10^6	2	72	11.5	2	κ_{Sem}
S5KsemA2F3	1.0	1.0	3.2×10^5	9.7×10^6	2	72	11.5	3	κ_{Sem}
			κ_{PLT} Series: Section 3.4						
S3KplA2F1	1.0	10.0	3.2×10^3	9.7×10^3	2	23	11.5	1	κ_{PL}
S4KplA2F1	1.0	3.2	3.2×10^4	3.1×10^5	2	40	11.5	1	κ_{PL}
S5KplA2F1	1.0	1.0	3.2×10^5	9.7×10^6	2	72	11.5	1	κ_{PL}
S6KplA2F1	1.0	0.3	3.2×10^6	3.1×10^8	2	128	11.5	1	κ_{PL}

Notes. The table is divided into subparts studying the dependence of our results on various cloud conditions (see the text) with a link to the section where each particular parameter series is presented. The fiducial run in our study is S5KsemA2F1. Columns in order indicate – Model: model name, M_{cloud}: mass of cloud, R_{cloud}: radius of cloud, Σ_{cloud}: mass surface density of the cloud given by $\Sigma_{\mathrm{cloud}} = M_{\mathrm{cloud}}/(\pi R_{\mathrm{cloud}}^2)$, n_{cloud}: number density of the cloud given by $n_{\mathrm{cloud}} = 3M_{\mathrm{cloud}}/(4\pi R_{\mathrm{cloud}}^3 m_{\mathrm{H}})$ where m_{H} is the mass of atomic hydrogen, α_{vir}: virial parameter under the assumption of a spherical cloud, σ_v: turbulent velocity dispersion of the cloud, $\mathcal{M}$: initial turbulent Mach number of the cloud, f_{DG}: dust-to-gas ratio enhancement factor over the solar value, κ_{R}: Rosseland opacity used in the model; where κ_{c} denotes a constant opacity whose value is provided, κ_{Sem} the Semenov opacity model (see Section 2.3), and κ_{PL} is the power-law opacity model from equation (16).

In order to ensure pressure equilibrium, we place the cloud in a lower density, hotter, ambient medium. The density and temperature contrasts are set such that $\rho_{\mathrm{cloud}} = \chi\,\rho_{\mathrm{ambient}}$ and $T_{\mathrm{cloud}} = \chi^{-1}\,T_{\mathrm{ambient}}$, with $\chi = 10^2$. We further initialize a mass scalar to represent the cloud material C_{cloud}, whose value lies between 0 and 1, representing purely ambient and cloud material, respectively. This allows us to set the correct thermal pressure for a mixture of cloud and ambient material at all times during the evolution. The thermal pressure P is then given by

$$P = c_{\mathrm{s}}^2 \rho\left[C_{\mathrm{cloud}} + \chi\left(1 - C_{\mathrm{cloud}}\right)\right]. \tag{17}$$

The side length of the cubic computational domain is set to $L = 4\,R_{\mathrm{cloud}}$, such that there is sufficient volume to track potentially expanding material (due to radiation feedback) before it leaves the domain through the boundaries.

We initialize the velocities in our clouds with supersonic turbulent fluctuations that follow a power spectrum $E(k) \propto k^{-2}$ (Federrath et al. 2010, 2021; Federrath 2013a) for $k/(2\pi/L) \in [2, 64]$, using the publicly available code by Federrath et al. (2022). We scale the magnitude of the fluctuations such that we obtain a target initial velocity dispersion σ_v, such that we obtain a target virial parameter (e.g. Federrath & Klessen 2012),

$$\alpha_{\mathrm{vir}} = \frac{2E_{\mathrm{kin}}}{E_{\mathrm{grav}}} = \frac{5R_{\mathrm{cloud}}\sigma_v^2}{3GM_{\mathrm{cloud}}}, \tag{18}$$

where $E_{\mathrm{kin}} = (1/2)M_{\mathrm{cloud}}\sigma_v^2$ and $E_{\mathrm{grav}} = (3/5)GM_{\mathrm{cloud}}^2/R_{\mathrm{cloud}}$. Most of our simulations use $\alpha_{\mathrm{vir}} = 2$, but we also vary this parameter in some cases; again, we provide a summary of all our simulations in Table 1.

We note that the initial turbulence imposed on the clouds, is not maintained by continuous driving, and is instead allowed to decay.[5] This misses the turbulent energy that might cascade from larger scales (effectively from the surrounding ISM, in which the cloud is embedded, but not included in our simulations), and could therefore give gravity an unfavourable advantage, leading to a higher star formation rate than would be expected in reality (see e.g. Lane et al. 2022). However, since our goal is to perform a controlled experiment to study the effects of radiation feedback, this matters little for our purpose, since even if our star formation rate is too high overall, we can still determine the relative efficiency of simulations with differing treatments of IR radiation.

We set the sound speed c_{s} such that the sonic Mach number $\mathcal{M} = \sigma_v/c_{\mathrm{s}} = 11.5$, identical to the value of $\mathcal{M}$ used by Skinner & Ostriker (2015). We note that the resulting values of c_{s} for most of our simulations are much higher than would be expected for the cold, dense, star-forming phase of the ISM that we are simulating.

---

[5]We note, however, that the gravitational collapse and radiation could itself drive turbulent motions over the course of the simulation.

Our choice is dictated largely by numerical convenience, since extremely large values of $\mathcal{M}$, as would be realistic for the clouds we are simulating, require extremely small hydrodynamic time-steps to remain numerically stable. As noted above, we do not expect this choice to matter significantly because the thermal pressure is negligible compared to the radiation pressure, making its exact value dynamically unimportant. We do not include magnetic fields in any of our simulations. We initialize the radiation field such that the initial radiation temperature is $T_r = T_{r,0} = 40$ K everywhere, and the radiation flux is zero.

We use diode boundary conditions for the hydrodynamics, i.e. gas is allowed to flow out of the domain, but not allowed to enter it. For the radiation moment equations, we adopt Marshak boundary conditions (Marshak 1958), such that the domain is bathed in a radiation field with temperature $T_{r,0} = 40$ K, but also allows radiation generated inside the domain to escape freely. Consistent with this choice, for the purpose of solving the time-independent RT equation (equation 13) for the Eddington tensor **T**, we set the intensity of rays entering the domain to a value given by the frequency-integrated Planck function evaluated at temperature $T_{r,0}$. This ensures that the boundary conditions in the two independent forms of the transfer equation solved by our scheme are consistent with each other, which has been shown to be important for stability and accuracy (e.g. Park et al. 2012; Davis et al. 2014).

2.5 Simulation suite

We run a range of simulations across parameter space to explore the role of the IR radiation pressure mechanism in different environments. The entire suite of simulations is summarized in Table 1. Our general naming convention for simulations is SsKkAaFf, where s, k, a, and f describe the surface density Σ, choice of opacity κ, virial parameter α, and dust-to-gas ratio relative to the solar value f_{dg} of the simulation; we explain values these parameters can take on in more detail below. We broadly divide the simulation suite as follows.

2.5.1 Idealized constant opacity runs

First, we run simulations with idealized, constant opacities, i.e. $\kappa_R = \kappa_c$, testing various values of κ_c. The intention of these idealized experiments is to compare with previous works (Skinner & Ostriker 2015; Tsang & Milosavljević 2018) and identify any differences. Since we use a more accurate method for radiation transport (VET) than earlier works, these simulations allow us to explore whether the RHD method has any effect on the results. In addition, these simulations also serve as a baseline to compare with our more physical, temperature-dependent opacity runs, and highlight how realistic opacities affect IR radiation feedback. For instance, although instabilities, such as the radiative Rayleigh–Taylor instability (RRTI), operate even for constant opacity laws (Jiang, Davis & Stone 2013), they are more pronounced for temperature-dependent opacity laws (Jacquet & Krumholz 2011; Krumholz et al. 2012a). For this series of runs, we perform seven simulations with values of $\kappa_c = 1, 2, 5, 10, 20, 40$ & 80. We use $M_{cloud} = 10^6$ M$_\odot$ and $R_{cloud} = 10$ pc for all the constant opacity runs, identical to the fiducial simulation of Skinner & Ostriker (2015). This corresponds to a value of $\rho_{cloud} = 1.6 \times 10^{-20}$ g cm^{-3}, and $\Sigma_{cloud} = 3.2 \times 10^3$ M$_\odot$ pc^{-2}. We use $\alpha_{vir} = 2$ for all these runs, which yields $\sigma_v = 23$ km s^{-1} and $c_s = 2$ km s^{-1} (see Section 2.4 for details). We discuss the results of these simulations in Section 3.1.

2.5.2 Milky Way-like dust opacity runs

Here we use more realistic, temperature-dependent IR opacities, which comprises the focus of our study. We explore the effects of such opacities across parameter space, with gas surface density Σ_{cloud} as the most important parameter. We test values of $\Sigma_{cloud} = 3.2 \times [10^3, 10^4, 10^5, 10^6]$ M$_\odot$ pc^{-2} with a Semenov et al. (2003) opacity law. The lowest Σ_{cloud} run has the same Σ as the fiducial run of SO15, while the latter two Σ values exceed the critical value Σ_{crit} estimated in C18; the former two are below the limit. Thus, this parameter exploration allows us to test the existence of – and possibly constrain – a value of Σ_{crit} above which IR radiation pressure might control ϵ_*. We obtain our target values of Σ_{cloud} by keeping the mass of the clouds fixed to $M_{cloud} = 10^6$M$_\odot$, and scaling R_{cloud} appropriately. We also tested alternative scalings to achieve a target Σ_{cloud} – by (i) keeping R_{cloud} fixed and modifying M_{cloud}, or (ii) keeping the ratio M_{cloud}/R_{cloud} fixed – and found that the evolution of the clouds between these scalings are indistinguishable. We retain $\mathcal{M} = 11.5$ and $\alpha_{vir} = 2.0$ – scaling σ_v and c_s appropriately, as outlined in Section 2.4. We use a value of $f_{dg} = 1$ for these simulations, i.e. Milky Way-like dust conditions, and refer to this series as the Σ_{cloud} series (Table 1). The results of these runs are summarized in Section 3.2.

We also run two simulations with values of $\alpha_{vir} = 3$ and 4, to test the effectiveness of feedback in (initially) unbound clouds. Such clouds may exist in starburst environments and extreme dynamical encounter regions, where large non-thermal motions may be driven by the high pressures and tidal forces in their environments. The names of these simulations are S5KsemAaF1, where the S5 notation indicates that these simulations have surface densities of 3.2×10^5 g cm^{-2}, and a can be either 3 or 4, indicating the value of the virial parameter. The results of these runs are summarized in Section 3.2.3.

2.5.3 Supersolar dust opacity runs

Since the dust opacity κ_R is the primary parameter of importance in determining the competition between gravity and feedback, it is interesting to consider supersolar, dust-enriched clouds, where radiation could play a more important role. It has been suggested in earlier, idealized (constant κ_R) simulations (SO15) that dust-enriched environments may reach high enough κ_R values to limit star formation. It is important to test if this is the case with a more realistic T-dependent κ_R, and if so, constrain the conditions where IR radiation feedback is able to significantly limit star formation. We emulate supersolar dust conditions with values of $f_{dg} > 1$, simply by scaling our default Semenov et al. (2003) opacities by f_{dg}, i.e. for $f_{dg} = 2$ we simply double the Milky Way-like opacity. We choose two values of Σ_{cloud} – one below the Σ_{crit} proposed in C18, i.e. $\Sigma_{cloud} = 3.2 \times 10^4$ M$_\odot$ pc^{-2}, and the other above, i.e. $\Sigma_{cloud} = 3.2 \times 10^5$ M$_\odot$ pc^{-2}. As we will see below, these cases also happen to be the most promising models in the Σ_{cloud}-series in terms of the potential of radiation pressure to compete against gravity. We test values of $f_{dg} = 2$ and 3, chosen roughly to match the metallicities (relative to solar) found in the most metal-rich galaxies (e.g. Curti et al. 2020). We refer to these simulations as the f_{dg} series (Table 1) and summarize the results of these experiments in Section 3.3.

2.5.4 Power-law approximation for T-dependent opacity runs

Finally, we repeat the Σ_{cloud} series with the κ_{PLT} power-law approximation for dust IR opacities. This approximation has been

adopted in the semi-analytic model of C18, which proposes the existence of a Σ_{crit}. It has also been adopted by earlier studies that explored the competition of IR radiation pressure and gravity with numerical simulations (e.g. Krumholz & Thompson 2012; Krumholz & Thompson 2013; Davis et al. 2014; Rosdahl & Teyssier 2015; Tsang & Milosavljević 2015; Zhang & Davis 2017).[6] These experiments allow us to determine the effects of adopting this approximation by comparing with the κ_{Sem} runs. We refer to these simulations as the κ_{PLT} series (Table 1) and describe their outcome in Section 3.4.

2.6 Resolution and numerical setup

All our simulations use a uniform grid (UG) resolution of $N = 256^3$ grid cells; for our domain of size $L = 4R_{cloud}$, this corresponds to a resolution $R_{cloud}/\Delta x = 64$. Although VETTAM supports AMR, we chose to use UGs here, motivated by a balance between accuracy and computational feasibility, considering the broad parameter space we intend to explore. Since we are primarily interested in the integrated star formation efficiencies set by the competition between gravity and feedback, and not in the detailed fragmentation properties or mass functions of the star clusters formed, we do not expect our grid resolution choice to be a major limitation. We verify this expectation in Appendix A3, where we describe convergence tests where we vary the dependence of our results on the UG resolution, and also compare to an AMR run with a maximum effective resolution of 1024^3 grid cells. We find that our results are reasonably converged at our fiducial resolution. We use a CFL number of 0.4 in our simulations, and a relative tolerance of 10^{-8} for our implicit update of the radiation moment equations. The solution to the time-independent transfer equation (equation 13) is performed with 48 rays per cell with our ray-tracing scheme, which uniformly samples angles on the unit sphere (using the healpix algorithm); however, we have also verified that using 192 angles yields nearly identical results. We run all simulations to a time $t = 8\,t_{ff}$, where t_{ff} is the free-fall time of the cloud, at which point nearly all mass has been accreted on to sinks or expelled from the computational domain by radiation forces, depending on the particular simulation model (see Table 1).

3 RESULTS

3.1 Idealized constant IR opacity clouds

Our first series of numerical experiments uses idealized constant opacities. We will not discuss these results in detail, since these runs simply repeat the earlier study of SO15, and differ only in the numerical method used and in that we extend their study to higher opacities.[7] The purpose of this set of simulations is to explore whether the results depend on the numerical method, and to serve as a baseline for comparison to our runs with a more realistic treatment of opacity. For this reason, we simply present the star formation efficiencies (ϵ_*;

---

[6]However, Tsang & Milosavljević (2015) deviate from a simple power-law at $T \sim 150$ K, capping the opacity at $\kappa_{PLT}(150)$

[7]SO15 were limited in the maximum opacity (and surface density) they could simulate by their explicit reduced-speed-of-light method for radiation, which becomes inaccurate in the dynamic diffusion regime, which is reached when the cloud optical depth is very large. The implicit Monte Carlo method used by Tsang & Milosavljević (2015) suffers from similar limitations, and in addition becomes very computationally expensive when the optical depth is large. Our VETTAM method does not suffer from these limitations; see Menon et al. (2022) for details.
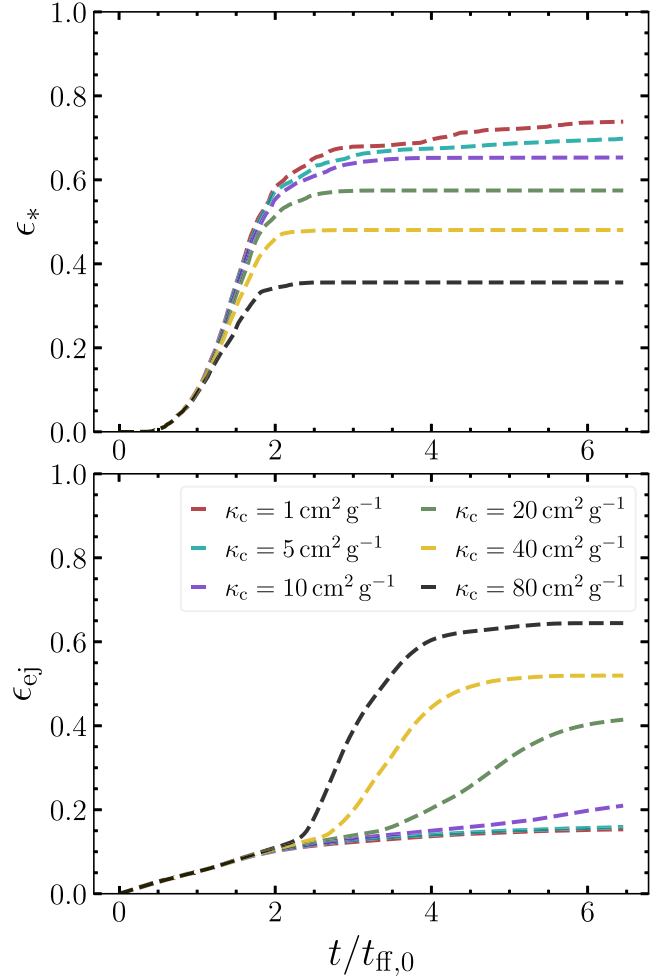
Figure 2. The star formation efficiency (ϵ_*;top-panel) and fraction of mass ejected from the simulation volume (ϵ_{ej};bottom-panel) for different values of κ_c (κ_c series; Table 1).

equation 1) and mass-ejection fractions obtained in our simulations for different values of κ_c, which can be compared to the earlier results. We show these quantities in Fig. 2. We find that, qualitatively, our conclusions mirror those of SO15, i.e. a constant dust opacity of $\kappa_c \gtrsim 20$ cm^2 g^{-1} is required for the IR radiation feedback to make more than a small difference in the final ϵ_*.

To provide a more direct quantitative comparison, we plot in Fig. 3 the ϵ_* we obtain at $t = 3\,t_{ff}$, as a function of κ_c, along with the values reported in table 2 of Skinner & Ostriker (2015) for the same quantity. We find that even quantitatively, the evolution of our clouds are very similar, suggesting that the M_1 radiation transport method used by SO15 does not yield results significantly different from our more accurate VET method for this particular setup. This is potentially because the limitations of the M_1 closure are more pronounced for regions close to the radiation sources, but do not play a significant role at larger distances, where the sources subtend a small solid angle (Kim et al. 2017). Since we are in the multiple-scattering regime, it is possible that the exact nature of the radiation field in the close vicinity of the sources is not crucial in determining the dynamical outcome. In addition, the shortcomings of the M_1 approximation are most significant in the presence of multiple sources of radiation acting in an optically thin medium. In the higher κ_c runs where radiation is dynamically important, the optical depths are >1 even in lower
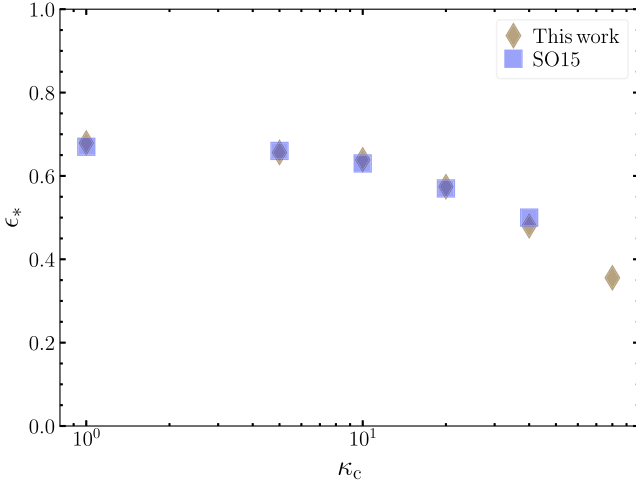
Figure 3. Comparison of ϵ_* values obtained in our study with those obtained in SO15. We can see that the outcomes are nearly identical.

density channels, so the M_1 method performs well. On the other hand, the radiation field in the lower κ_c runs could be (significantly) affected by whether M_1 or VET is used; however, in these runs radiation forces are subdominant compared to gravity in any event, and thus inaccuracies in computing them do not change the basic outcome. Therefore, we caution that the similarity in outcomes with the M_1 and VET closure in these idealized simulations should not be generalized.[8]

3.2 Milky way-like dust conditions

3.2.1 Evolution of models

Next we summarize the evolution of clouds with the fiducial initial conditions, i.e. $f_{\rm dg} = 1$, $\alpha_{\rm vir} = 2$, and $\Sigma = 3.2 \times 10^3 - 3.2 \times 10^6 \, {\rm M}_\odot \, {\rm pc}^{-2}$ and our full treatment of temperature-dependent opacities ($\Sigma_{\rm cloud}$ series; Table 1). As an example of the results for these models Fig. 4 shows snapshots of the surface density in run S5KsemA2F1 at times $[1, 3, 5, 7] t_{\rm ff}$. We can see that the initial turbulent velocity fluctuations lead to a highly filamentary structure, where self-gravitating overdensities form star clusters. The self-gravity of the gas, combined with the gravity from the point sources, leads to global collapse of the cloud, increasing the total sink mass and hence ϵ_*. We find that by $\sim 7 \, t_{\rm ff}$, the star formation efficiency reaches $\epsilon_* \approx 75$ per cent, with the remainder of the gas mass supported by systematic rotation seeded by the initial velocity fluctuations and then amplified by angular momentum conservation during the collapse. A central cluster is formed, with the highest mass sink particle sinking to the central regions. In addition, we see that the dynamical interaction between the star clusters leads to some of the lower mass clusters being pushed out to larger radii. It is clear that overall, the radiation pressure is unable to prevent accretion, or to drive winds that are dynamically significant.

We find that the evolution of clouds for all other $\Sigma_{\rm cloud}$ cases are qualitatively similar to that shown in Fig. 4. We compare the

---

[8]For instance, in the single-scattering UV radiation pressure context, Kim et al. (2017) – who use an adaptive ray-tracing method (which is expected to be of similar accuracy to the VET) – compare their results with Raskutti et al. (2016), and show that the radiation pressure is underestimated with the M_1 approximation, leading to a higher final ϵ_*.
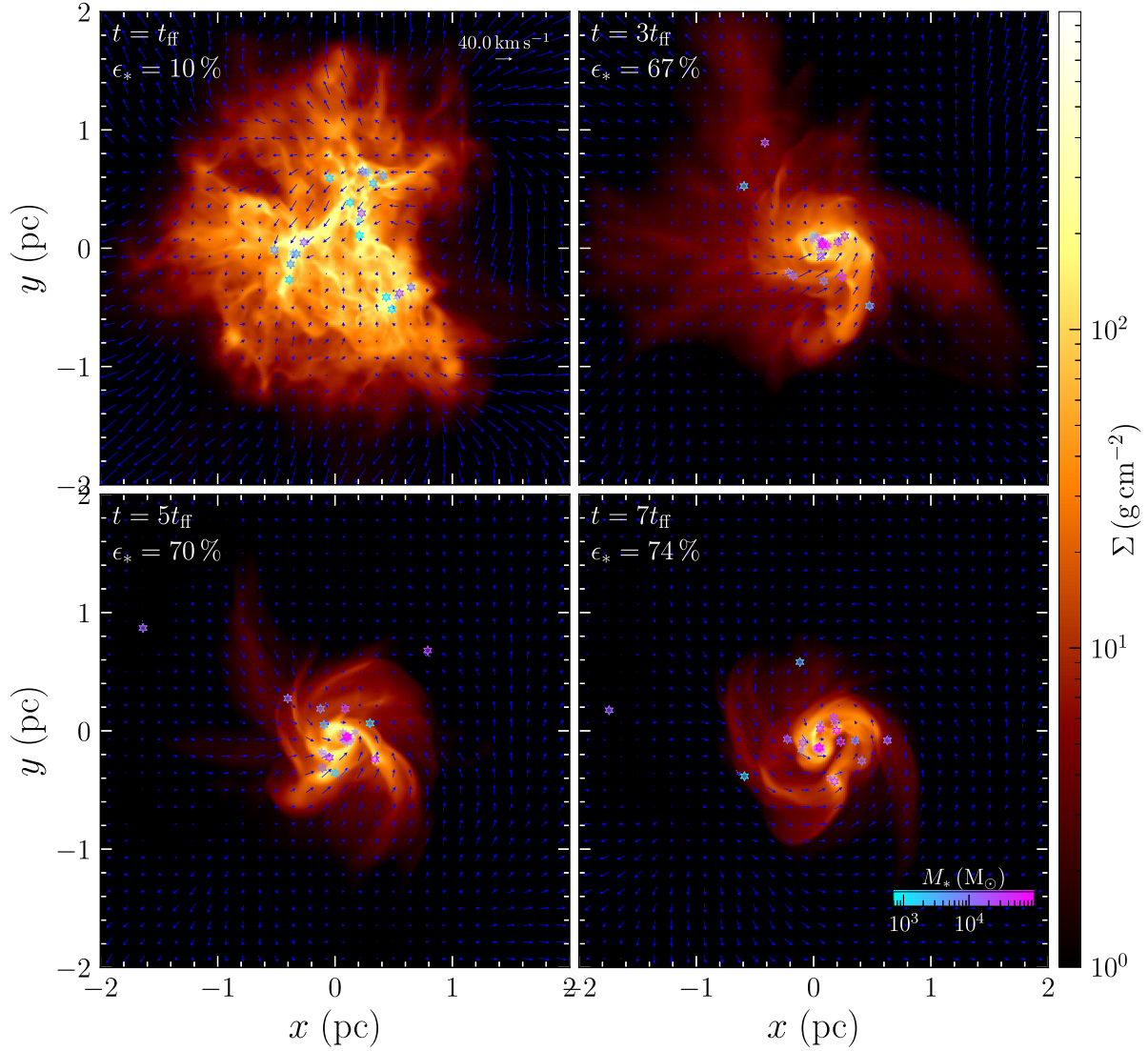
projected surface densities for runs S3KsemA2F1, S4KsemA2F1, S5KsemA2F1, and S6KsemA2F1 at $t = 7 \, t_{\rm ff}$ in Fig. 5. We can see that, when we normalize positions to the initial cloud radius and surface densities to the initial cloud surface density, the final states of these cases are qualitatively identical.

To explore this more quantitatively, in Fig. 6 we show the time evolution of the integrated star formation efficiency ϵ_*, and the fraction of mass ejected from the simulation domain $\epsilon_{\rm ej}$, for the four values of $\Sigma_{\rm cloud}$ illustrated in Fig. 5. We can see that the curves are nearly identical to one another, and to a control run without radiation. This clearly establishes that the radiation forces are unable to affect the dynamical outcomes of the clouds. In all cases ϵ_* rises sharply with time, starts to slow down by $t \sim 2 \, t_{\rm ff}$, and by $t \sim 3 \, t_{\rm ff}$ reaches $\epsilon_* \sim 80$ per cent, with mass continuing to accrete at a very slow rate (as indicated by the positive slope) thereafter. Most of the remaining matter escapes from the simulation domain, $\epsilon_{\rm ej} \sim 20$ per cent, but this escape is due to the initial turbulence and not the IR radiation pressure, as evidenced by a saturation at later times and by the fact that $\epsilon_{\rm ej}$ is nearly identical in the control run and the radiation runs.

3.2.2 Comparison of radiation and gravity forces

To understand the balance of forces in the problem, and arrive at a physical explanation for the simulation outcomes, we compare the two dominant competing forces: radiation pressure and gravity. We examine the force balance as a function of radius using a method similar to that of Skinner & Ostriker (2015). For a given snapshot in time, we define a spherical coordinate system centred on the instantaneous centre of mass of the sink particles, and assign every computational cell to one of 128 radial bins relative to this point. We then compute the mean (specific) radial component of the radiation force, and the competing (specific) radial gravitational force (combination of gas self-gravity and sink particles), in each bin by averaging over all solid angles. We denote these averages by $\langle \ldots \rangle_{4\pi}$. Formally, we define the mean radiation force as

$$\langle \dot{p}_{\rm rad} \rangle_{4\pi} = \left\langle \frac{\kappa_{\rm R} \boldsymbol{F}_0}{c} \cdot \hat{\boldsymbol{r}} \right\rangle_{4\pi}, \tag{19}$$

where $\boldsymbol{F}_0$ is the radiation flux in the co-moving frame of the fluid, which can be obtained from the lab-frame radiation flux to $\mathcal{O}(v/c)$ by the relation (e.g. Castor 2004),

$$\boldsymbol{F}_0 = \boldsymbol{F} - E_r \boldsymbol{v} \cdot (\mathbf{I} + \mathbf{T}), \tag{20}$$

and $\hat{\boldsymbol{r}}$ is the unit vector in the radial direction in the coordinate system defined by the sink particles' centre of mass. To understand the radial variations of $\langle \dot{p}_{\rm rad} \rangle_{4\pi}$ in further detail, we also separately compute the radially averaged radiation flux $F_{\rm r} = \langle \boldsymbol{F}_0 \cdot \hat{\boldsymbol{r}} \rangle_{4\pi}$, the radially averaged Rosseland opacity $\langle \kappa_{\rm R} \rangle_{4\pi}$, and the radially averaged radiation temperature $\langle T_{\rm r} \rangle_{4\pi}$. The corresponding (specific) gravitational force $\langle \dot{p}_{\rm grav} \rangle_{4\pi}$ is given by

$$\langle \dot{p}_{\rm grav} \rangle_{4\pi} = \langle g_{\rm gas} \rangle_{4\pi} + \langle g_* \rangle_{4\pi}, \tag{21}$$

where $g_{\rm gas} = -\hat{\boldsymbol{r}} \cdot \nabla \Phi_{\rm gas}$, $g_* = -\hat{\boldsymbol{r}} \cdot \nabla \Phi_*$, and $\Phi_{\rm gas}$ and Φ_* are the gravitational potentials of the gas and sink particles, respectively (we note that the sink particle potential is softened at radii of $r < 2.5 \, \Delta x$ to prevent diverging values near the centre of the sink particle; see Federrath et al. 2010c). We can use these relations to compute the ratio of these forces, i.e. the Eddington ratio $f_{\rm Edd}$ at each point, given by

$$f_{\rm Edd} = \frac{\dot{p}_{\rm rad}}{\dot{p}_{\rm grav}}, \tag{22}$$

Figure 4. Surface density maps for model (S5KsemA2F1) at t/t_{ff} = 1, 3, 5, 7 with the corresponding star formation efficiency (ϵ_*) annotated. The star symbols indicate sink particles, coloured by their mass. Vectors (blue) indicate the mass-weighted projected velocity field, with arrow length indicating velocity magnitude. The scale for the velocity vectors is annotated in the top left-hand panel.

and average this quantity at each radial shell to obtain the volume-averaged Eddington ratio $\langle f_{\mathrm{Edd}}\rangle_r$.

In Fig. 7 we show the radial variation of $\langle f_{\mathrm{Edd}}\rangle_r$ (top panel), $\langle T_r\rangle_{4\pi}$ (middle panel), and $\langle\kappa_R\rangle$ (bottom panel) obtained for the different Σ_{cloud} models. We see from the top panel that $\langle f_{\mathrm{Edd}}\rangle_r < 1$ for all the models, which explains why the results are nearly identical in all cases: the dynamics are dominated by $\langle\dot{p}_{\mathrm{grav}}\rangle_{4\pi}$, which is (once we normalize out the cloud size) more or less independent of Σ_{cloud}. However, this does not yet explain what drives the differences in $\langle f_{\mathrm{Edd}}\rangle_r$ across the models, and thus, why radiation is subdominant compared to gravity. There are clear differences in the values of $\langle f_{\mathrm{Edd}}\rangle_r$ for different Σ_{cloud}, with higher Σ_{cloud} cases reaching, on average, higher values of $f_{\mathrm{Edd}}\rangle_r$, but also reaching their maxima at different locations. These differences cannot be driven by differences in the radiation flux, which on the grounds of energy balance must always be close to $L/(4\pi r^2)$, independent of Σ_{cloud}; direct examination of the flux confirms this conclusion. Instead, as the middle and bottom panels of Fig. 7 show, differences in the radiation force are primarily driven by how $\langle T_r\rangle_{4\pi}$, and the corresponding

$\langle\kappa_R\rangle_{4\pi}$ (which depends on T_r) vary with radius. While $\langle T_r\rangle_{4\pi}$ varies as roughly $r^{-0.5}$ in all cases, the normalizations of the different Σ_{cloud} runs are very different: higher Σ_{cloud} leads to higher $\langle T_r\rangle_{4\pi}$, consistent with the expectation that there is enhanced trapping of photons at higher Σ_{cloud}. This drives complex, non-monotonic variations in $\langle\kappa_R\rangle_{4\pi}$, due to the non-trivial dependence of the κ_{Sem} opacity law on T_r (see Fig. 1). The mean opacity varies smoothly and almost monotonically with radius for the models with lower values of Σ_{cloud}, but for the cases with higher Σ_{cloud}, $\langle\kappa_R\rangle_{4\pi}$ has a distinct peak at which $\langle\kappa_R\rangle_{4\pi} \sim 6\,\mathrm{cm}^2\,\mathrm{g}^{-1}$, and falls at radii on either side of this peak. This occurs due to the drop in κ_R at larger temperatures in the κ_{Sem} opacity law.

3.2.3 Dependence on virial parameter

Here, we compare the evolution of clouds with our fiducial setup at different values of the initial virial parameter α_{vir}, testing values of $\alpha_{\mathrm{vir}} = 3$ and 4, compared to the fiducial value of 2. These runs allow us to explore whether radiation can drive winds from more
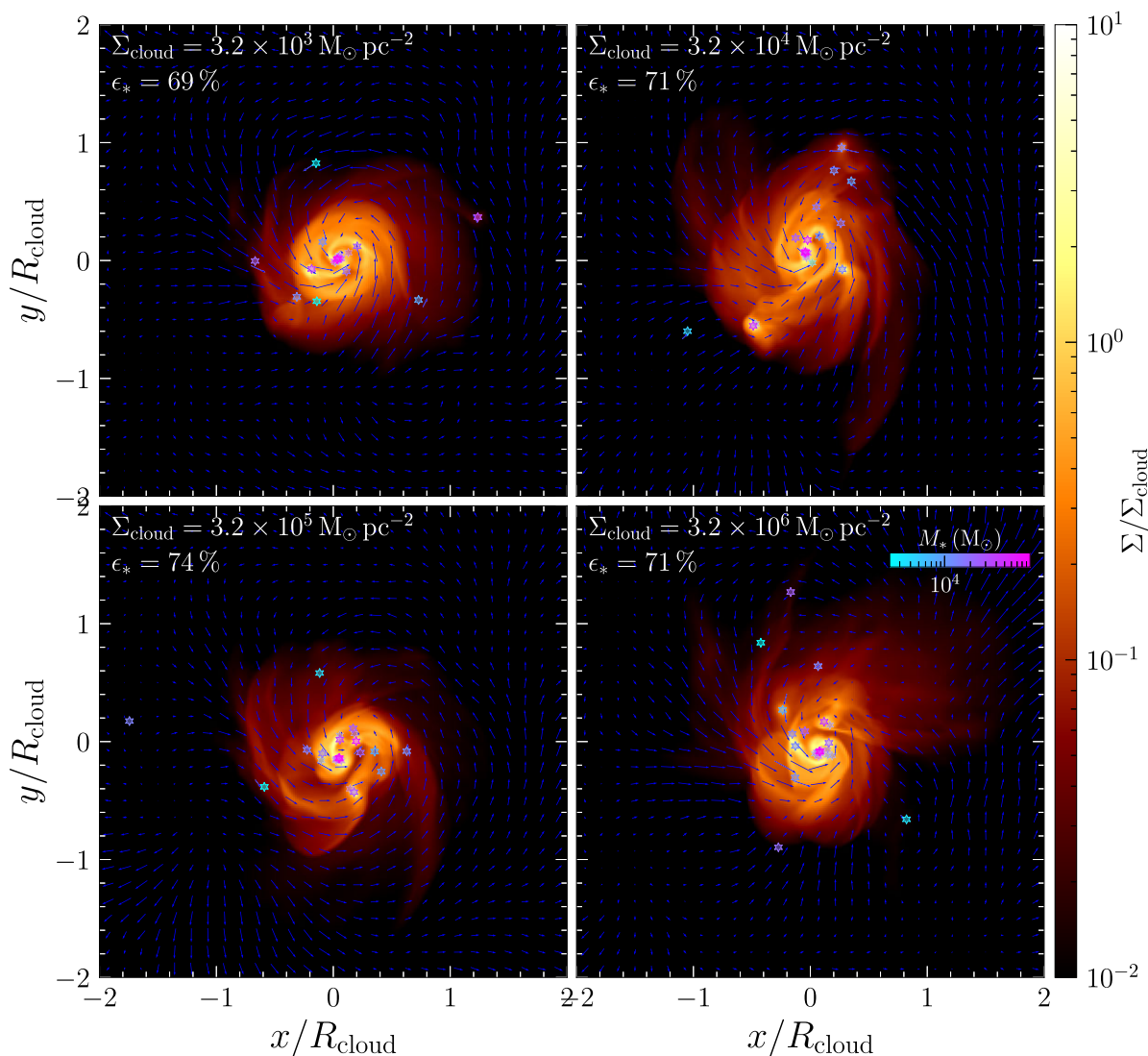
Figure 5. Same as Fig. 4, but now the four panels show results for different values of $\Sigma_{\rm cloud}$ at $t = 7t_{\rm ff}$, and with surface densities and positions scaled to Σ_0 and $R_{\rm cloud}$, respectively.

weakly bound clouds. However, in Fig. 8 we see that this is not the case. We find that ϵ_* is lower, and $\epsilon_{\rm ej}$ higher, in runs with higher $\alpha_{\rm vir}$, with $\epsilon_* \sim 70$ per cent and 60 per cent in the $\alpha_{\rm vir} = 3$ and 4, respectively. However, this difference is entirely driven by the fact that the dominance of turbulence over gravity leads to expansion and loss of gas from the clouds, as demonstrated by the fact that the control runs without radiation yield nearly indistinguishable curves in Fig. 8. Thus, even for clouds that are largely unbound, IR radiation feedback is unable to affect their dynamical evolution. This, along with the results of the previous sections, implies that the effects of IR radiation feedback are unambiguously negligible in regulating star formation for solar-neighbourhood dust conditions. We note, however, that the higher $\alpha_{\rm vir}$ runs, although initially unbound, eventually become bound due to the decay of turbulence. This is demonstrated in a plot of $\alpha_{\rm vir}$ (calculated using equation 18) with time in Fig. 9. It is possible that IR radiation might be more effective in an environment where the turbulence is driven by a cascade from larger scales (e.g. Federrath, Klessen & Schmidt 2008), rather than freely decaying.

3.3 Supersolar dust conditions

Next, we present the results of our runs with supersolar dust conditions, i.e. values of $f_{\rm dg} > 1$. In Fig. 10 we compare the evolution of ϵ_* and $\epsilon_{\rm ej}$ over time for the different runs. The cases with $f_{\rm dg} = 1$ and 2 reach final values of ϵ_* that are indistinguishable, suggesting that radiation is still largely subdominant in these cases. Even with a higher value ($f_{\rm dg} = 3$) the effects on ϵ_* (and $\epsilon_{\rm ej}$) remain minor. Despite being small, these differences are worth investigating in order to gain physical insight. First consider the case $\Sigma_{\rm cloud} = 3.2 \times 10^4\,{\rm M_\odot\,pc^{-2}}$, $f_{\rm dg} = 3$, which deviates from the other cases at $t \sim 2t_{\rm ff}$, after which star formation slows down, eventually saturating at $\epsilon_* \sim 70$ per cent, slightly lower than the $\epsilon_* \sim 80$ per cent attained by the corresponding $f_{\rm dg} = 1$ case. Differences in $\epsilon_{\rm ej}$ are substantially smaller than for ϵ_*, suggesting that radiation pressure is sufficient to inhibit star formation, but not to eject gas completely for this run. Interestingly, the $\Sigma_{\rm cloud} = 3.2 \times 10^5\,{\rm M_\odot\,pc^{-2}}$ run, which showed the greatest promise for radiation in the $f_{\rm dg} = 1$ runs (see Fig. 7), shows weaker radiation effects at $f_{\rm dg} = 3$ case than the $\Sigma_{\rm cloud} = 3.2 \times 10^4\,{\rm M_\odot\,pc^{-2}}$ case.
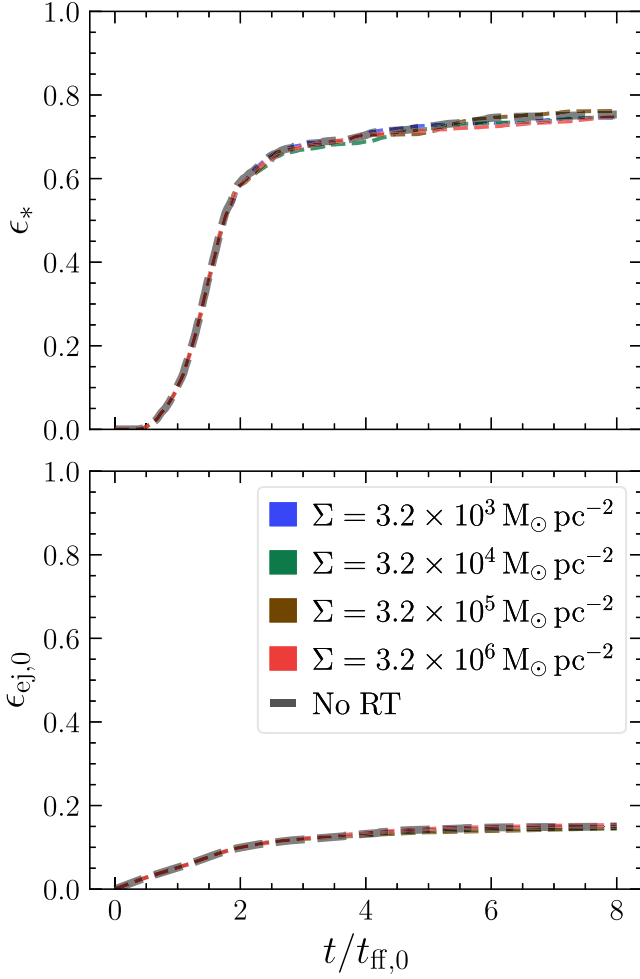
Figure 6. Time evolution of quantities compared for different values of Σ (colours). The dark grey dashed lines indicate a control run without radiation feedback (No RT). Top: the integrated star formation efficiency ($\epsilon_* = M_*/M_{\rm cloud}$), Bottom: the fraction of mass ejected from the computational volume ($\epsilon_{\rm ej} = M_{\rm ej}/M_{\rm cloud}$, where $M_{\rm ej}$ is the ejected mass).

To understand this behaviour, we again construct radial profiles of the volume-weighted Eddington ratio $\langle f_{\rm Edd} \rangle_{4\pi}$ as a function of radius r for these runs, which we show in Fig. 11. We see that higher $f_{\rm dg}$ yields larger $\langle f_{\rm Edd} \rangle_{4\pi}$, as expected, but for $f_{\rm dg}$ values of 1 (as shown earlier) and 2, the profiles are sub-Eddington over all r, explaining why radiation does not modify the evolution of these models at all. The $f_{\rm dg} = 3$ cases, however, shows signs of trans- and even super-Eddington profiles at some radii, although they remain sub-Eddington over most of the cloud. In the $\Sigma_{\rm cloud} = 3.2 \times 10^4\,{\rm M}_\odot\,{\rm pc}^{-2}$ model, this occurs very close to the sinks, indicating that radiation provides support against gravity in these regions. We confirm that gas is flowing away from the sinks locally at small r in this simulation by plotting $\langle v_r \rangle_{4\pi}$ – the radial profile of the volume-weighted average radial velocity of gas – in Fig. 12. However, outflow is restricted to the polar directions, and accretion continues to occur along dense, optically thick filaments, very similar to the configuration found in simulations of the formation of individual massive stars (e.g. Krumholz et al. 2009; Kuiper et al. 2012; Rosen et al. 2016). Moreover, even the gas that is driven outwards at small radii does not escape, as is clear both from the reversal of $\langle v_r \rangle_{4\pi}$ at larger radii, and from the fact that $\epsilon_{\rm ej}$ does not increase in this run even though
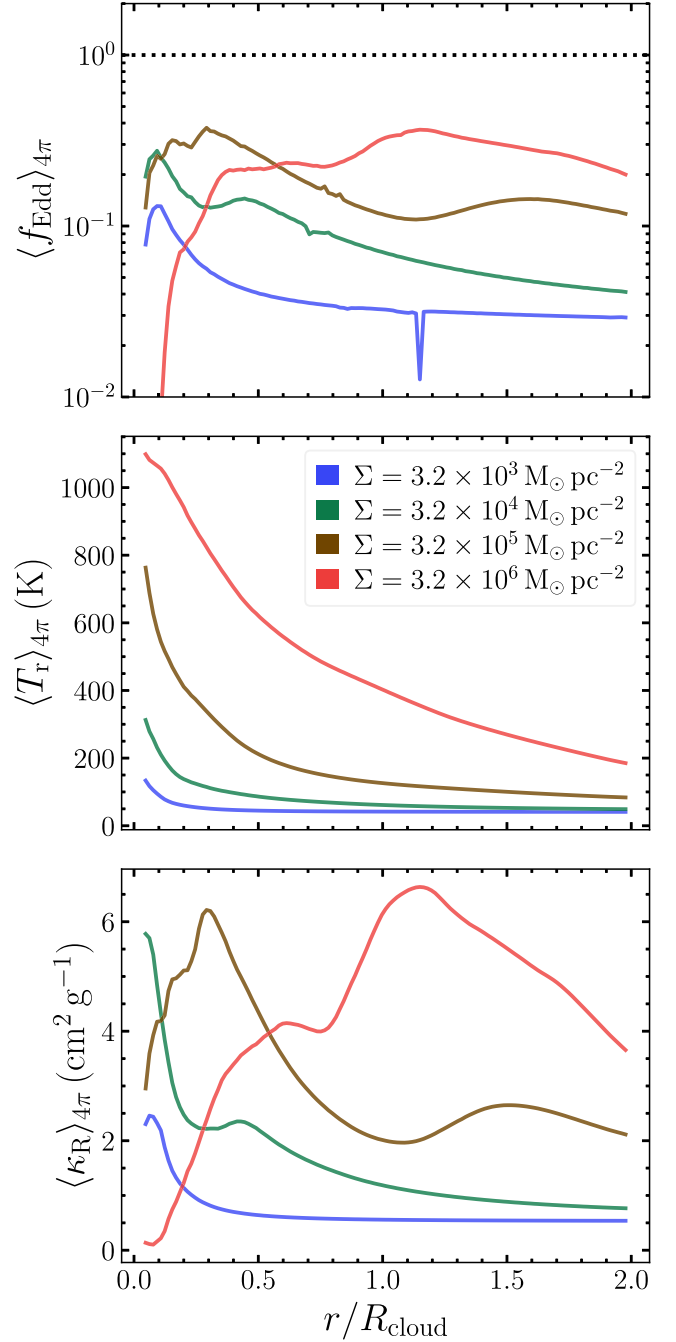
Figure 7. Balance of forces, and the physical properties that control it, compared for different $\Sigma_{\rm cloud}$. The top panel shows the volume-weighted Eddington ratio $f_{\rm Edd}$, i.e. the ratio between radiation and gravitational forces (equation 22) with the dotted line indicating $\langle f_{\rm Edd} \rangle_{4\pi} = 1$. The middle panel shows the averaged radiation temperature T_r, and the bottom panel shows the averaged Rosseland opacity ($\kappa_{\rm R}$).

ϵ_* declines. This is because such gas eventually reaches larger radii, where it sees a cooler radiation field and becomes sub-Eddington. It is also noteworthy that, although the case $\Sigma_{\rm cloud} = 3.2 \times 10^5\,{\rm M}_\odot\,{\rm pc}^{-2}$ also reaches $\langle f_{\rm Edd} \rangle_{4\pi} > 1$, for this run radiation is less effective at reducing ϵ_* than in the case of lower surface density. This suggests that it matters where the gas is super-Eddington; closer to the sinks yields more regulation of star formation.
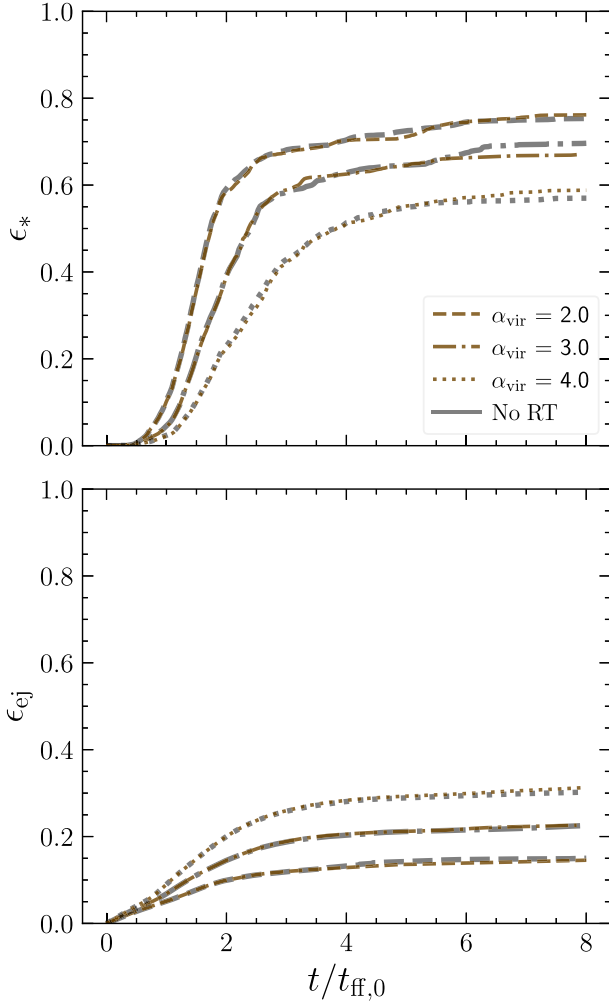
Figure 8. Same as Fig. 6 for $\Sigma = 3.2 \times 10^5 \, \mathrm{M_\odot \, pc^{-2}}$, but for different values of the initial virial parameter of the cloud (α_{vir}). While the final SFE responds to changes in α_{vir}, due to turbulence expanding the clouds, radiation feedback does not play any significant role in this process, as demonstrated by the three control runs (one for each α_{vir}) without radiation (grey lines).
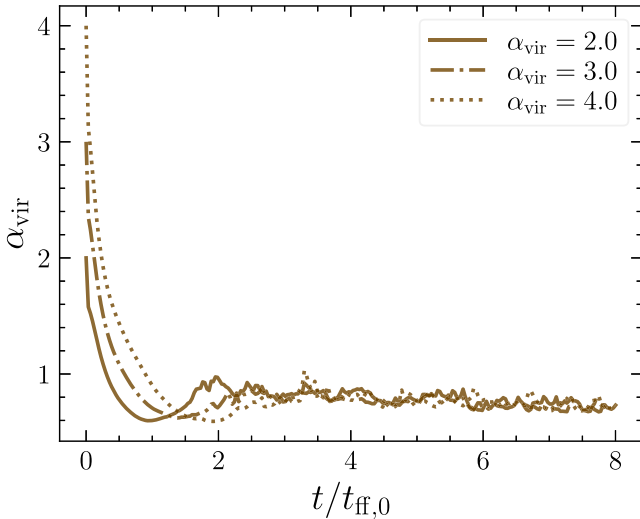
Figure 9. Time evolution of α_{vir} for the runs with different initial cloud virial parameters. We can see that even the initially supervirial clouds (i.e. $\alpha_{\mathrm{vir}} = 3$ and 4) eventually reach subvirial states, and saturate to $\alpha_{\mathrm{vir}} \lesssim 1$.
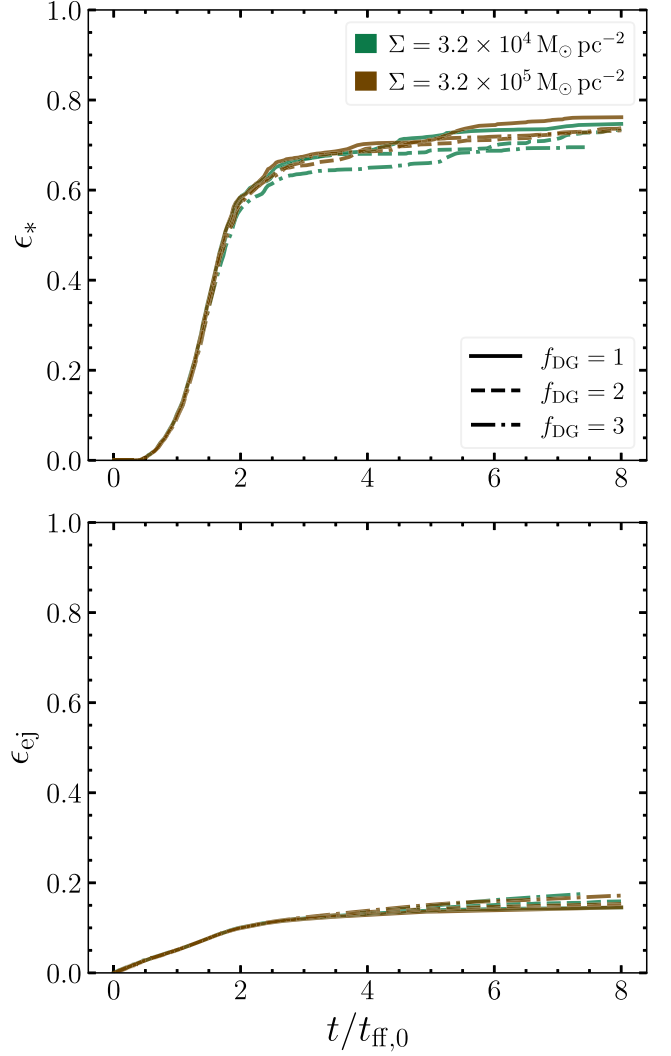
Figure 10. Same as Fig. 6, but for different values of the relative dust-to-gas ratio compared to solar conditions (f_{dg}).

Overall, our models indicate that even for the most metal-rich observed systems, IR radiation feedback is unlikely to be significant.

3.4 Power-law opacities

In our final set of experiments, we quantitatively compare the time evolution of clouds with the κ_{Sem} and κ_{PLT} opacity laws; as discussed in Section 2.5.4, the latter is a simplification commonly adopted in both simulations and semi-analytic models. In Fig. 13, we plot ϵ_* and ϵ_{ej} as a function of time for the different values of Σ_{cloud}. As discussed in earlier sections, the cases with κ_{Sem} opacities are qualitatively identical to one another and to a control run without radiation. On the other hand, the cases with the κ_{PLT} opacity law show a strong anticorrelation between ϵ_* and Σ_{cloud} – with the exception of the $\Sigma_{\mathrm{cloud}} = 3.2 \times 10^6 \, \mathrm{M_\odot \, pc^{-2}}$ case, to which we shall return below. This exception aside, we find that for cases with higher Σ_{cloud}, ϵ_* saturates at earlier times and reaches much lower final values. The bottom panel of Fig. 13, which shows the time evolution of ϵ_{ej}, demonstrates that this is because these runs drive winds that escape the domain, which is not the case for the κ_{Sem} runs. Interestingly, the transition to IR radiation ejecting > 50 per cent of the initial mass
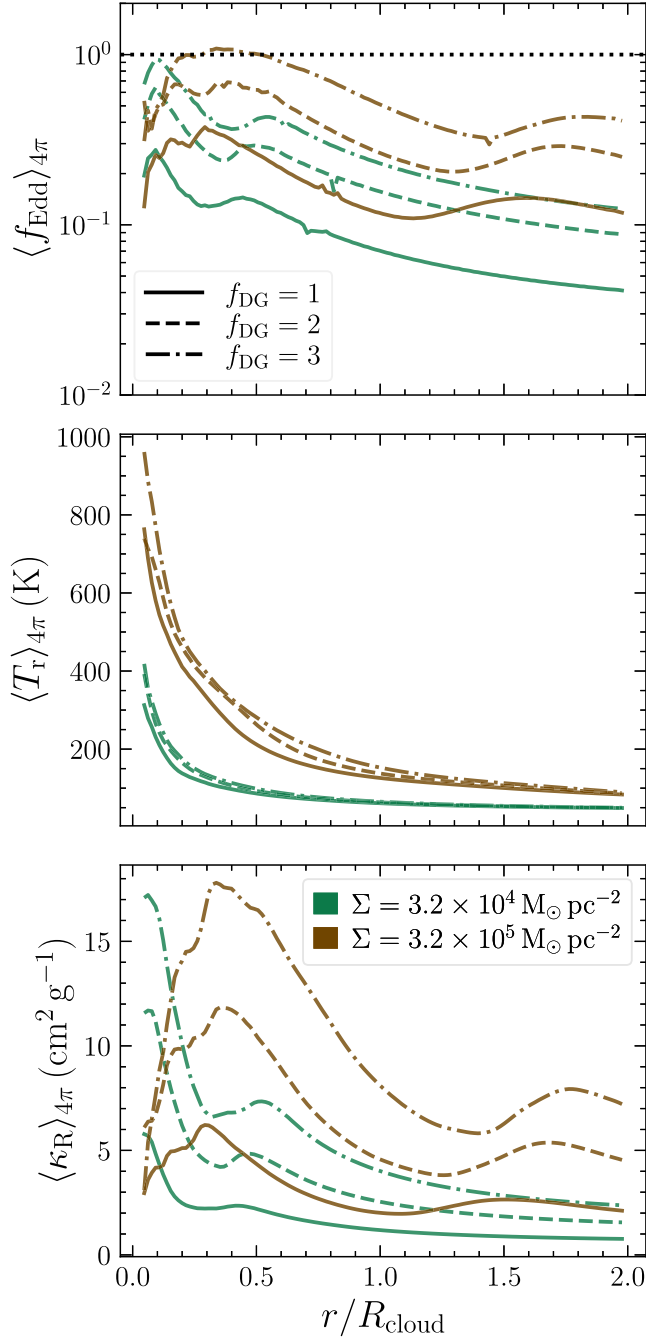
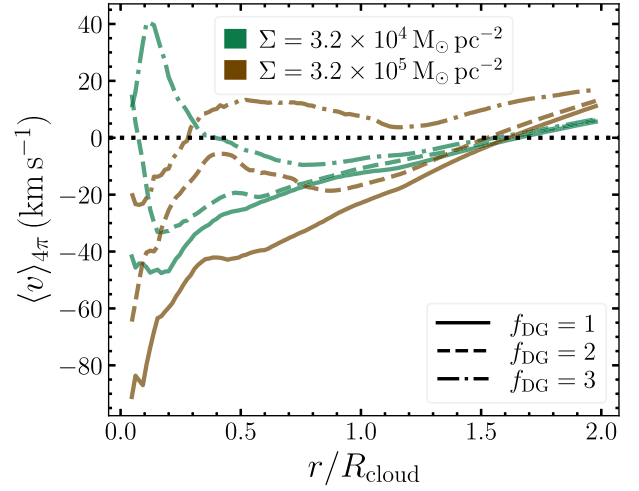**Figure 11.** Same as Fig. 7, but for different f_{dg}.

Figure 12. Volume-weighted radial profiles of the radial gas velocity (v_r) for the runs with different f_{dg}.
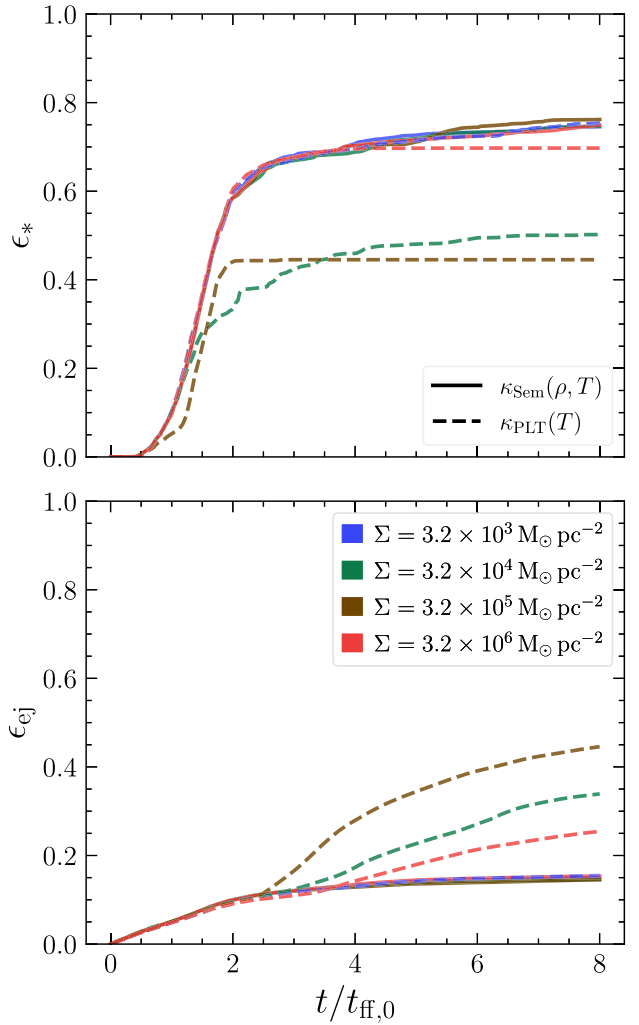

Figure 13. Same as Fig. 6, but for runs using the Semenov et al. (2003) IR opacities (κ_{Sem}; solid lines), and the power-law approximation to the IR opacities (κ_{PLT}; dashed lines) for the different values of Σ.
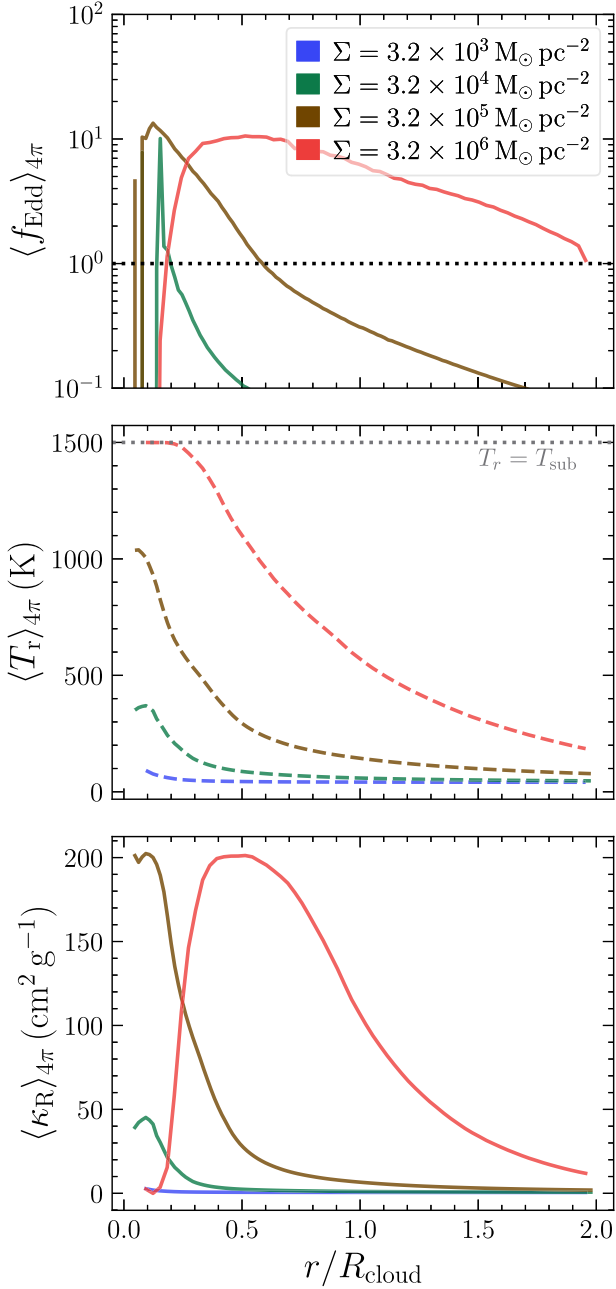
occurs at roughly 10^5 M$_\odot$ pc^{-2}, in good agreement with the critical value derived by C18 using the power-law opacity approximation.

To understand why the κ_{PLT} models are so different from the κ_{Sem} ones, we look at the radial profiles of T_r, κ_R and f_{Edd} for the κ_{PLT} models in Fig. 14. We can compare this with Fig. 7 for the κ_{Sem} runs. We see that at higher Σ_{cloud} – which corresponds to higher values of T_r near the clusters – $\kappa_{PLT} \gg \kappa_{Sem}$, rendering the system super-Eddington. The $\Sigma_{cloud} = 3.2 \times 10^4$ M$_\odot$ pc^{-2} case is super-Eddington only in a small region close to $r = 0$, while the $\Sigma_{cloud} = 3.2 \times 10^5$ M$_\odot$ pc^{-2} case is super-Eddington over much of the cloud volume, at both small and large radii. Similar to the S4KsemA2F3 run discussed in the previous section, this leads to increasing regulation of star formation, but not complete suppression,

Figure 14. Same as Fig. 7, but for runs using the $\kappa_{\rm PLT}$ opacity law (equation 16). Note that the dotted grey line in the middle panel indicates the dust sublimation temperature ($T_{\rm sub}$) beyond which $\kappa_{\rm R} = 10^{-3}$. We see that the $\kappa_{\rm PLT}$ approximation severely overestimates $\kappa_{\rm R}$ for the higher $\Sigma_{\rm cloud}$ runs compared to the $\kappa_{\rm Sem}$ opacities (see Fig. 7), thereby producing super-Eddington states. This explains why the $\kappa_{\rm PLT}$ model significantly impacts ϵ_*, whereas the $\kappa_{\rm Sem}$ is unable to.

since accretion can still continue through opaque channels. The plot also explains why the $\Sigma_{\rm cloud} = 3.2 \times 10^6 \, {\rm M_\odot \, pc^{-2}}$ is an exception to the trend of lower ϵ_* with higher $\Sigma_{\rm cloud}$: it is because a significant fraction of volume has $T_{\rm r} > 1200$ K, which leads to very low values of $\kappa_{\rm R}$ due to dust sublimation for radii $r/R_{\rm cloud} \lesssim 0.3$; thus the deviation from the trend found elsewhere in the PLT models for this run lies in the fact that it is not exactly a power law, but instead deviates from this behaviour at sufficiently high $T_{\rm r}$.

Thus we find that the power-law approximation significantly overestimates the effects of IR radiation pressure. We discuss the implications of this finding for earlier numerical results in Section 4.2.

4 DISCUSSION

4.1 Why is IR radiation feedback dynamically unimportant?

The most important conclusion obtained from the simulations presented in the last section is that IR radiation pressure is unable to compete with gravitational forces, and as a result, plays a negligible role in controlling the star formation efficiency of clouds. This holds across a wide range in $\Sigma_{\rm cloud}$ ($\sim 10^3$–$10^6 \, {\rm M_\odot \, pc^{-2}}$), and even at dust-to-gas ratios (relative to solar) up to ~ 3, in disagreement with the qualitative expectations of semi-analytical studies (Thompson et al. 2005; Murray et al. 2010; Crocker et al. 2018). To understand why this is the case, we explore two possible mechanisms: (1) an anticorrelation between radiation flux and matter density, which is a critical mechanism in the formation of individual massive stars (Krumholz et al. 2009; Rosen et al. 2016) and has been suggested to be of importance for young stellar populations as well (e.g. Jacquet & Krumholz 2011; Krumholz et al. 2012a; Davis et al. 2014), and (2) the fact that the IR dust opacities are never high enough for radiation forces to matter (Fig. 1 and Semenov et al. 2003). We explore the role of both effects in detail below.

4.1.1 Radiation–matter anticorrelation

Fig. 15 provides visual evidence of radiation–matter anticorrelation: the flux has higher magnitude (indicated by longer vectors) in optically thinner channels, indicating that the radiation force is strongest where there is less matter and weakest where there is more matter. We quantify the extent of the anticorrelation by computing the correlation fraction of the specific opacity $\rho \kappa_{\rm R}$ and the flux $F_{\rm r}$, given by

$$\chi_{\rho \kappa_{\rm R}, F_{\rm r}} = \frac{\langle \rho \kappa_{\rm R} F_{\rm r} \rangle_{4\pi}}{\langle \rho \kappa_{\rm R} \rangle_{4\pi} \langle F_{\rm r} \rangle_{4\pi}}. \tag{23}$$

A value of $\chi_{\rho \kappa_{\rm R}, F_{\rm r}} = 1$ indicates that the fluctuations of $\rho \kappa_{\rm R}$ and $F_{\rm r}$ are uncorrelated, whereas $\chi_{\rho \kappa_{\rm R}, F_{\rm r}} < 1$ indicates anticorrelations in the fluctuations about the mean. We compare the radial profiles of $\chi_{\rho \kappa_{\rm R}, F_{\rm r}}$ for the different $\Sigma_{\rm cloud}$ models in Fig. 16. We find anticorrelation in all the model clouds, with the strongest anticorrelation at small radii (also visible in the slice plots of Fig. 15, which shows a disc-like structure close to the star through which the radiation flux is low), and at higher $\Sigma_{\rm cloud}$. These two trends suggest that the increase of $\kappa_{\rm R}$ found at higher $\Sigma_{\rm cloud}$ and smaller radii is balanced to an extent by an increased level of radiation–matter anticorrelation.

4.1.2 Dust opacities

To isolate the effects of realistic dust opacities from the radiation–matter anticorrelation, we ask whether radiation forces in a spherically symmetric cloud – one where by construction there can be no radiation–matter anticorrelation, can be dynamically important if $\kappa_{\rm R} = \kappa_{\rm Sem}$. For a spherical cloud in steady state, the radiation transport equations, equations (5) and (6), reduce to a pair of ordinary differential equations that govern the run of radiation quantities through the cloud, and which can be solved given a density profile $\rho(r)$ and a radiation source term (given by equation 15) for a source at $r = 0$. We solve these equations for a cloud of mass $M_{\rm cloud} = 10^6 \, {\rm M_\odot}$,
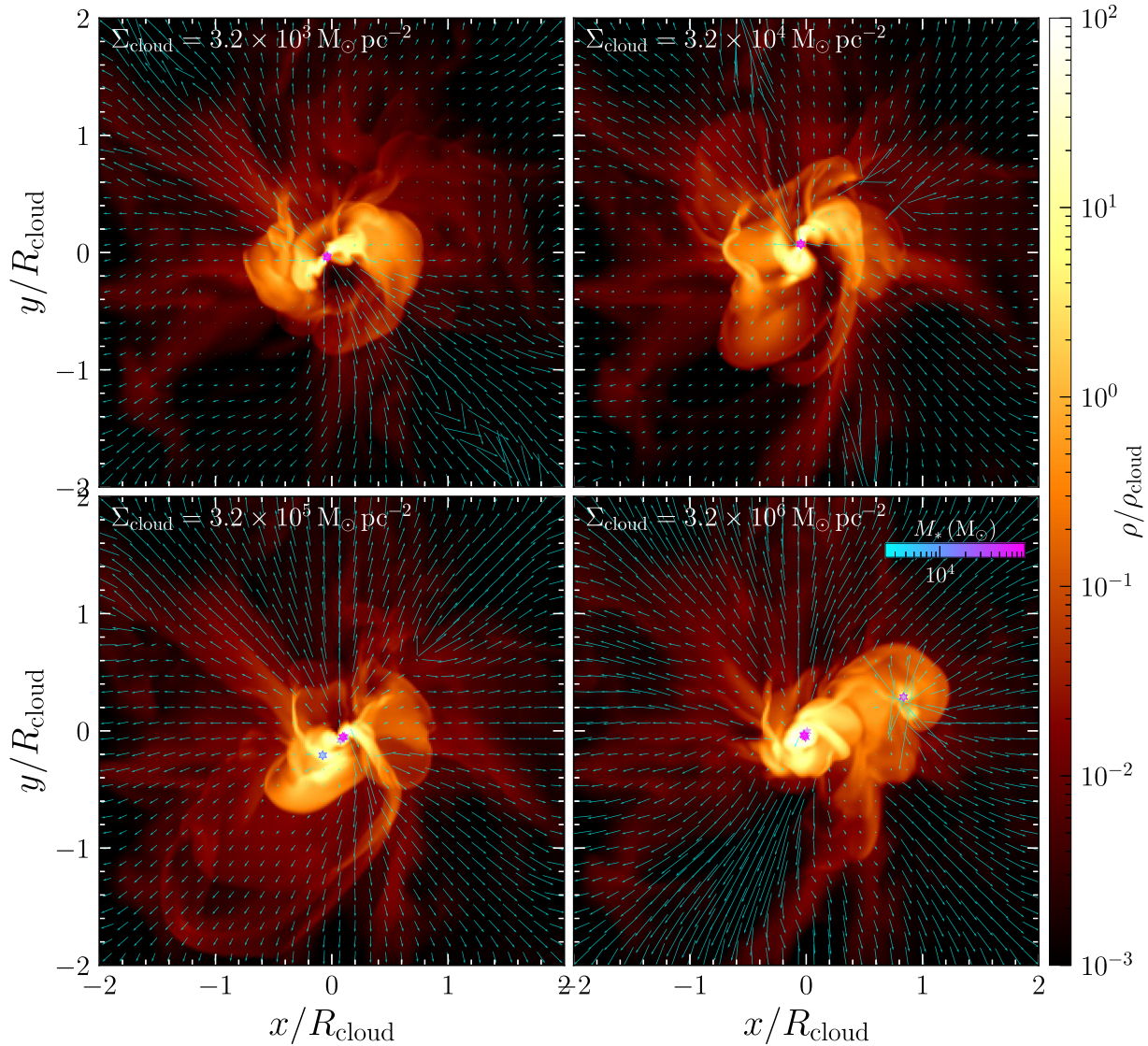
Figure 15. Comparison of slices of the gas density in the $x - y$ plane, for the runs with different $\Sigma_{\rm cloud}$ ($\kappa_{\rm Sem}$ series; Table 1) at $t = 5t_{\rm ff}$. The slice is centred on $x = y = 0$, $z - z_{*,\rm max}$ where $z_{*,\rm max}$ is the z-coordinate of the sink with highest mass in each run. Star symbols indicate sink particles, coloured by their mass. Vectors (cyan) indicate the radiation flux field, scaled by r^2 to account for its geometrical dilution. We can visually identify that there is an anticorrelation between the radiation flux and matter density to some level in all four cases, with high values of flux in rarer regions and almost negligible in the dense filamentary structures near the stars.

and a mass in stars of $M_* = \epsilon_* M_{\rm cloud}$. For our numerical solution we adopt $\epsilon_* = 0.7$, chosen to approximately match the steady-state conditions attained by our models at solar dust conditions (see Fig. 6), but the results are qualitatively similar for other choices. Given these fixed conditions, we can parametrize our models in terms of just two parameters: the mass surface density Σ, and a power-law index α such that $\rho(r) \propto r^{-\alpha}$. The complete description of the model, and our numerical approach to solving the resulting equations, are provided in Appendix B. We test values of Σ that correspond to the four $\Sigma_{\rm cloud}$ values used in our various simulations ($\kappa_{\rm Sem}$ series; Table 1), and values of $\alpha = 0$, 1, and 2; the results prove to be almost completely insensitive to α, and hence we do not show the variation with α here.

In Fig. 17, we directly show the Eddington ratio $f_{\rm Edd}$ calculated from the steady-state distributions of radiation energy, flux and opacities in our models; we show profiles of these quantities in Fig. B1 of the Appendix. We show the profiles for a range of $\Sigma_{\rm cloud}$ at $f_{\rm dg} = 1$,

and for $f_{\rm dg} = 2$ and 3 for the fiducial $\Sigma_{\rm cloud} = 3.2 \times 10^5$ M$_\odot$ pc^{-2}. We can see that irrespective of the value of $\Sigma_{\rm cloud}$, $f_{\rm Edd} < 1$ for $f_{\rm dg} = 1$. In fact $f_{\rm Edd}$ is at most ~ 0.5 for the fiducial $\Sigma_{\rm cloud}$ case, reasonably close to the ranges found in the full 3D numerical simulations (see Fig. 7). At $f_{\rm dg} \sim 3$, there is a small range of radii with $f_{\rm Edd} > 1$, but most of the volume remains sub-Eddington. This strongly suggests that the inability of the radiation to dynamically alter the state of the clouds is driven by the dust opacity – even with perfect radiation-matter coupling, radiation forces are subdominant compared to gravity.

4.1.3 Relative importance of dust opacities and radiation-matter anticorrelation

It is now interesting to ask which of these mechanisms is the more important contributor to keeping the radiation forces in our simulations sub-Eddington. The fact that we find $f_{\rm Edd} < 1$ even in the
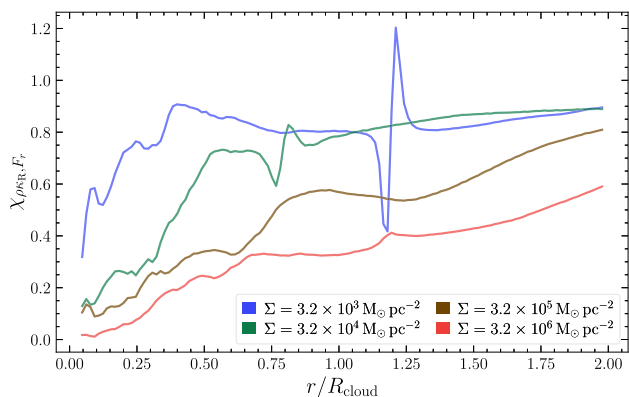
Figure 16. Correlation fraction $\chi_{\rho\kappa_R, F_r}$ (equation 23) of the specific opacity $\rho\kappa_R$ and the radial flux F_r for the runs from Fig. 15. We can see that there is significant radiation flux–matter anticorrelation, and increasingly so at higher Σ.
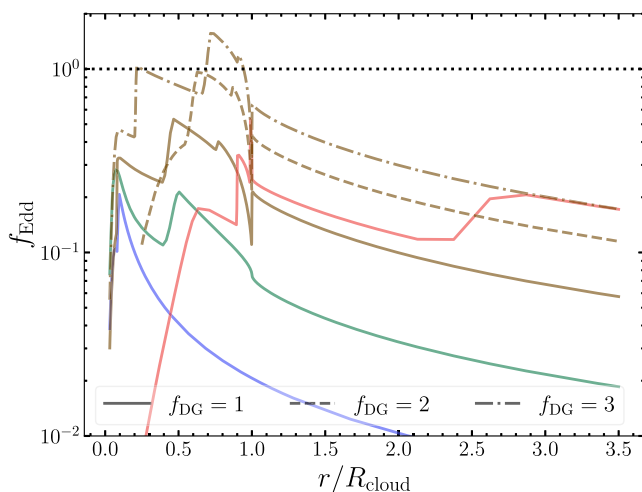

Figure 17. The Eddington ratio obtained with the idealized, steady-state model described in Section 4.1.2. Colours indicate the four Σ_{cloud} values as in previous figures. The dashed and dash-dotted lines indicate $f_{dg} = 2$ and 3, respectively. The horizontal dotted line indicates $f_{Edd} = 1$, i.e. a balance between radiation and gravity forces. We see that $f_{Edd} < 1$ in all the cases with solar f_{dg}, indicating that even without matter–radiation anticorrelation, radiation forces are unlikely to compete with gravity. Even for $f_{dg} = 3$, only a small radial region has $f_{Edd} \gtrsim 1$.

spherically symmetric models suggests that the opacities alone are sufficient at $f_{dg} = 1$; although there is radiation–matter anticorrelation ($\chi_{\rho\kappa_R, F_r} < 1$), it does not change the qualitative results, as evidenced by the similar values of f_{Edd} found in our simulations (Fig. 7) and the spherically symmetric models (Fig. 17).

However, radiation–matter anticorrelation becomes increasingly important when the opacities permit radiation forces to approach the Eddington limit; this can be seen in the larger differences between the spherically symmetric models and the simulations at higher f_{dg}, and in the constant opacity runs (Section 3.1), and in the smaller values of $\chi_{\rho\kappa_R, F_r}$ found at higher Σ_{cloud}. It is also apparent in the quantitative outcomes of the simulations: for constant κ_c, a spherically symmetric cloud becomes super-Eddington once its star formation efficiency exceeds (Fall et al. 2010, SO15)

$$\epsilon_* = \frac{4\pi G c}{\kappa_c \langle L_*/M_* \rangle}. \tag{24}$$

For our highest opacity case, $\kappa_c = 80\,\mathrm{cm^2\,g^{-1}}$, this expression yields $\epsilon_* = 0.17$, whereas our simulation (S3K80A2F1) reaches $\epsilon_* \sim 0.4$; more generally, this expression predicts a relation $\epsilon_* \propto 1/\kappa_c$, significantly steeper than the observed relationship (c.f. Fig. 3). The flattening at high κ_c is due to radiation–matter anticorrelation becoming increasingly effective lowering the mass-weighted Eddington ratio relative to the naive spherically symmetric estimate as κ_c increases.

In summary, we find that at solar conditions, the IR opacities rule out the possibility of radiation pressure being dynamically important at all for objects whose light-to-mass ratios are in the range expected for fully sampled stellar populations with a standard IMF (as opposed to single massive stars or top-heavy IMFs). However, even where radiation forces are enhanced – such as metal-rich regions with higher $f_{dg} > 1$, or around objects with higher $\langle L_*/M_* \rangle$ – radiation–matter anticorrelation kicks in to reduce the effectiveness of feedback. We note, however, a subtle point: while the radiation–matter anticorrelation can (significantly) reduce the effectiveness of feedback in instances where the conditions permit super-Eddington states, it cannot reduce it sufficiently to render the system sub-Eddington altogether – there is still some level of mass-loss driven by radiation. This can, for instance, be seen in our runs with $f_{dg} = 3$. Thus anticorrelation does not alter the conditions where IR radiation becomes dynamically important, rather, it just reduces the effectiveness of radiation forces once those conditions are satisfied. This echoes the picture outlined in the idealized experiments of IR radiation pressure in gravitationally confined columns of Davis et al. (2014), where the condition for radiation-driven instability is the same as that derived by Krumholz & Thompson (2012), and once instability begins, anticorrelation acts to reduce the effectiveness of feedback, but steady winds are none the less still driven by radiation pressure. Our primary new finding here is that, for realistic rather than idealized opacities, stellar populations with normal IMFs embedded in a solar neighbourhood-like ISM will never cross the instability threshold in the first place.

4.2 Implications for earlier studies of radiation–matter interaction using approximate opacities

One of the interesting insights offered by our study is the importance of adopting realistic, temperature-dependent dust IR opacities (e.g. Semenov et al. 2003) in models of IR radiation feedback; commonly used alternatives such as an idealized constant opacity or a power-law (κ_{PLT}) approximation to the Semenov et al. (2003) opacities can lead to qualitatively different conclusions due to their tendency to overestimate the radiation forces. This finding has important implications for earlier studies in the literature that rely on approximate opacities.

A set of studies have explored the role of IR radiation pressure in the context of driving (large-scale) dusty winds in starbursts and rapidly star-forming environments (see, Zhang 2018, for a review). This was first studied in models of dusty columns of matter confined in a gravitational field by Krumholz & Thompson (2012) (KT12 hereafter). They described the parameters of the models in terms of the dimensionless numbers $f_{E,*}$ and τ_*: the (area-averaged) Eddington ratio of the system and the Rosseland mean optical depth of the slab of gas, respectively. They then derived a maximum Eddington ratio $f_{E,crit}(\tau_*)$ for which such a slab can be in hydrostatic equilibrium, and used simulations to explore the behaviour of slabs beyond this stability limit. Subsequent studies (Davis et al. 2014; Rosdahl & Teyssier 2015; Tsang & Milosavljević 2015; Zhang &

Davis 2017) confirmed the stability limit, but found that the KT12 simulations, which relied on the flux-limited diffusion approximation, underestimate the radiation forces, which leads to qualitatively different behaviour in models that lie in certain regions of parameter space (Davis et al. 2014; Zhang & Davis 2017). However, some of these studies use the κ_{PLT} approximation for their dust opacities, which we show in Section 3.4 to significantly overestimate the radiation forces and lead to qualitatively different conclusions than the more realistic dust opacities provided by Semenov et al. (2003). This is fundamentally due to the significantly higher κ_R with the κ_{PLT} power law, which even at modest temperatures of $\sim 200\,K$ can lead to ~ 2 times higher κ_R, with the discrepancy getting progressively worse at higher temperatures (see Fig. 1).

A similar point can be made about another popular approach, which has been to adopt a constant (but high) opacity for IR photons; for example, Hopkins, Quataert & Murray (2011, 2012), Bieri et al. (2017), Costa et al. (2018), and Hopkins (2018) all adopt $\kappa_c = 10\,cm^2\,g^{-1}$. A comparison to Fig. 7 shows that, even for extremely high surface densities, the maximum opacity in any radial bin is a factor of two smaller. In addition, the volume average is a factor of 3–4 smaller, since the opacity drops with radius, as the spectrum gets redshifted (i.e. lower T_r). This point has previously been made by Reissl et al. (2018), and our findings here confirm this.

This finding calls into question the results of the aforementioned models, primarily for cases with $\tau_* \gg 1$, i.e. models with more trapping of radiation, and hence higher (mid-plane) temperatures. For instance, fig. 9 of Krumholz & Thompson (2013) shows that the mid-plane temperature in their run with $\tau_* = 10, f_{E,*} = 0.5 > f_{E,crit}(\tau_* = 10)$ can be $\sim 400\,K$ using their dimensional scaling.[9] This corresponds to κ_R values that are a factor ~ 5 larger with the κ_{PLT} opacity than the corresponding κ_{Sem} opacities at the same temperature. Indeed, based on our findings it is likely that a system with these parameters would not be unstable using the correct opacities. It is therefore important to revisit the conditions for driving a wind in the $\tau_* > 1$ regime with the κ_{Sem} opacities, and/or recompute the numerical simulations with them. This is especially relevant as the conditions on $f_{E,*}$ and τ_* for driving a wind are used to infer the plausibility of radiation pressure driving powerful dusty winds in ULIRGs and starburst galaxies (e.g. section 4.2 in Zhang & Davis 2017), which observations suggest can reach $\tau_* \sim 30$ (Barcos-Muñoz et al. 2017). It has been assumed that this is sufficient to trigger IR radiation-driven winds, but our results suggest a need to revisit this conclusion.

4.3 Trapping of infrared radiation

Subgrid models and observations of IR radiation feedback are frequently expressed in terms of the IR radiation trapping factor, f_{trap}, defined as the ratio of the net momentum imparted to the gas by IR photons to the momentum flux carried by the direct stellar radiation field,

$$\dot{p}_{rad,tot} = (1 + f_{trap})L_*/c, \tag{25}$$

where $\dot{p}_{rad,tot}$ is the total momentum per unit time transferred to the gas, and L_* the luminosity of the star cluster. The factor of 1 in the above equation is the momentum imparted by the absorption of the direct (UV) photons from the star, and f_{trap} indicates the factor by

which this is boosted due to the radiation pressure on dust by IR photons trapped in the opaque cloud. Spherically symmetric semi-analytic models suggest values of $f_{trap} \sim 4$–5 (e.g. Murray, Quataert & Thompson 2010) for gas conditions similar to massive clusters in the Milky Way, but SO15 find in their 3D simulations that these models can overestimate f_{trap} by a factor of ~ 5 due to their inability to include radiation-gas anticorrelation. That said, SO15 use idealized constant opacities, which we have shown can yield misleading results, and they only explore clouds with relatively low values of Σ_{cloud}. It is therefore of interest to investigate f_{trap} in our simulations, and their implications for both subgrid models and for the interpretation of observations.

4.3.1 The trapping factor

We obtain f_{trap} from our simulations by directly computing the cumulative momentum imparted to gas by radiation pressure over the extent of the cloud, and taking the ratio of this to the momentum flux carried by the radiation field (i.e. L_*/c). The cumulative momentum imparted is given by integrating $\langle \dot{p}_{rad} \rangle_{4\pi}$ over spherical shells through the cloud, which gives

$$f_{trap}(r) = \frac{\int_0^r \langle \dot{p}_{rad} \rangle_{4\pi} 4\pi r^2 dr}{L_*/c}. \tag{26}$$

Here the numerator is the rate of momentum deposition in gas out to radius r. For comparison, we also compute the cumulative optical depth through the cloud, given by

$$\tau_{IR}(r) = \int_0^r \langle \rho \kappa_R \rangle_{4\pi} dr, \tag{27}$$

where $\langle \rho \kappa_R \rangle_{4\pi}$ is the averaged specific opacity over all solid angles. This quantity represents the value of f_{trap} that would be expected if our gas cloud were spherically symmetric and had the same radial opacity distribution as our simulated clouds. Thus, if $f_{trap} < \tau_{IR}$, this indicates radiation-matter anticorrelation.

We show the radial profiles of f_{trap} and τ_{IR} in Fig. 18. We see that f_{trap} and τ_{IR} both saturate at $r \sim 0.3\,R_{cloud}$, suggesting that most of the momentum is imparted in the regions close to the star clusters. We find that τ_{IR} is larger than f_{trap} by about a factor ~ 10, with larger differences at larger Σ_{cloud}, pointing to coupling of the radiation to matter that is somewhat inefficient at low Σ_{cloud} and becomes increasingly inefficient as Σ_{cloud} increases, consistent with our findings above. However, in spite of the anticorrelation, f_{trap} is significantly higher than unity at higher Σ_{cloud}.

4.3.2 Implications for subgrid models

Our finding that $f_{trap} > 1$ raises the following question: if high values of f_{trap} are possible, why do they not affect the dynamical state of the cloud, and what are the implications of this finding for semi-analytic models of IR radiation feedback where the strength of feedback is parametrized by f_{trap}? After all, semi-analytical models (Thompson et al. 2005; Hopkins et al. 2010; Murray et al. 2010), and numerical simulations that adopt versions of them (Hopkins et al. 2011, 2012), find momentum-driven expansion of their model clouds even at modest f_{trap} values of ~ 10. Why do our simulations have $f_{trap} > 10$ in some cases, yet IR feedback has no effect?

This question can be addressed by comparing the trapped IR momentum budget (i.e. $f_{trap}L_*/c$) with the momentum per unit time provided by the gravitational force. We quantify this by calculating

---

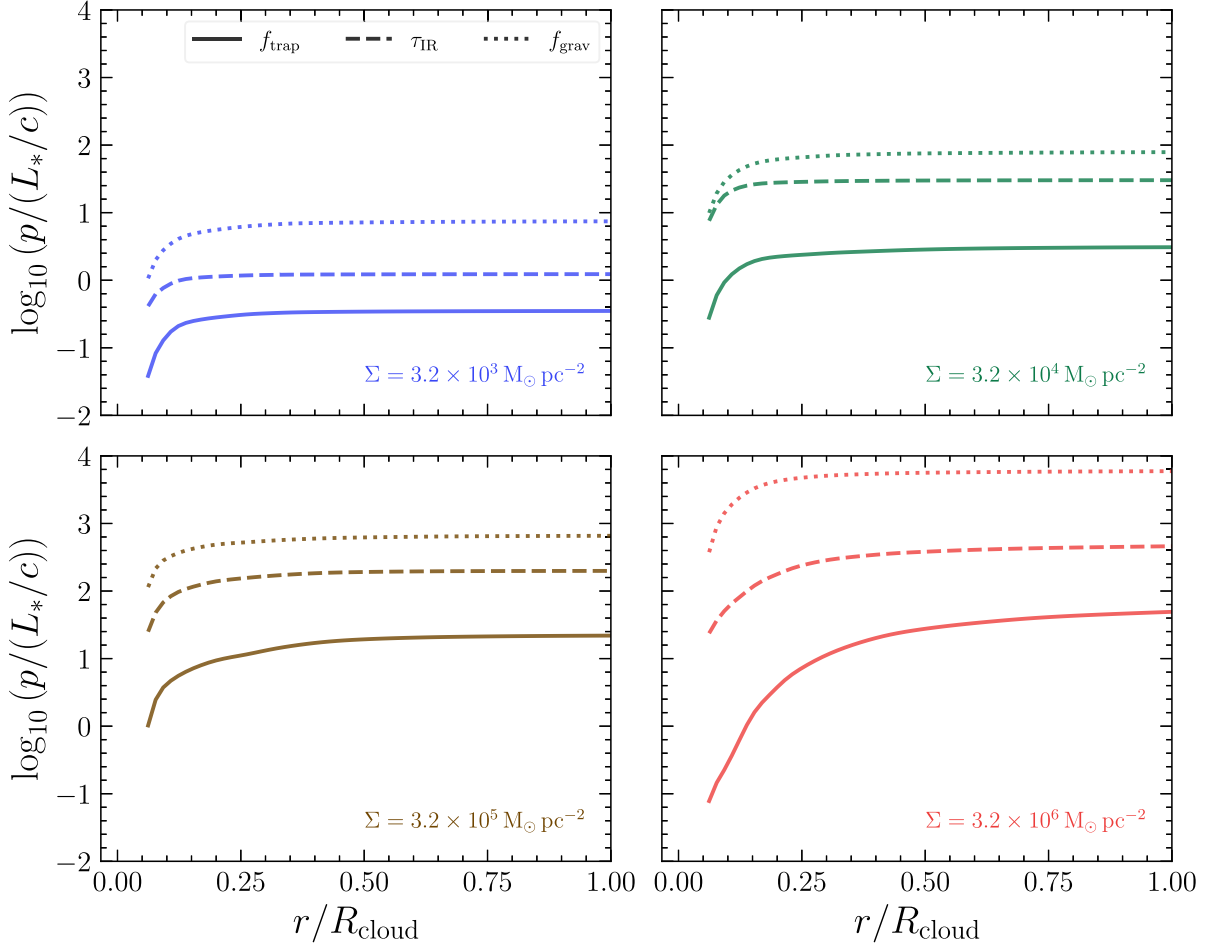[9]The temperatures could be systematically higher in these simulations since they neglect gravity; however, even in the corresponding run with gravity in KT12, the temperatures were $\sim 300\,K$.

Figure 18. Comparison of the cumulative trapping factor ($f_{\rm trap}$; equation 26) in solid lines, the cumulative IR optical depth ($\tau_{\rm IR}$; equation 27) in dashed lines, and the (scaled) cumulative momentum imparted by gravity ($f_{\rm grav}$; equation 28) shown as dotted lines, for different $\Sigma_{\rm cloud}$ shown in different panels. $f_{\rm trap}$ and $\tau_{\rm IR}$ respectively quantify the cumulative IR radiation momentum imparted to the gas in our simulations, and the cumulative momentum that would have been imparted if the cloud were spherically symmetric and had identical average radial profiles of the specific opacity $\rho\kappa_{\rm R}$; the difference between them arises primarily due to the radiation-matter anticorrelation. However, we also note that even $\tau_{\rm IR}$ is lower than $f_{\rm grav}$.

an effective gravity momentum, in analogy to equation (27),

$$f_{\rm grav}(r) = \frac{\int_0^r \langle \dot{p}_{\rm grav}\rangle_{4\pi} 4\pi r^2 {\rm d}r}{L_*/c}, \tag{28}$$

where $\dot{p}_{\rm grav}$ is the change in gas radial momentum per unit time per unit volume due to gravitational forces. This quantity is directly comparable to $f_{\rm trap}(r)$, in that it describes the momentum per unit time imparted to gas at radius $<r$ by gravitational forces, again normalized to the momentum flux of the direct stellar radiation field. We overplot $f_{\rm grav}$ in Fig. 18. We can see that $f_{\rm grav}$ exceeds $f_{\rm trap}$ at all r, explaining why even very high values of $f_{\rm trap}$ need not lead to winds driven by radiation pressure – higher $f_{\rm trap}$ comes with even higher $f_{\rm grav}$. This is not surprising, and is just another way of stating the point that gravitational forces dominate over the radiation pressure for all r in our clouds; in such a picture, it does not matter that $f_{\rm trap}$ is very large, because $f_{\rm grav}$ is always larger.

However, this finding has an important implication for subgrid models applied to simulations that do not resolve the competition of radiation pressure and gravity: such simulations should not impart momentum with ad-hoc values of $f_{\rm trap}$ – even ones that are calibrated to 3D simulations that resolve the radiation feedback, such as ours. This is due to the fact that, since $f_{\rm grav} > f_{\rm trap}$, the gas that absorbs

the trapped photon momentum gets accreted back to the sources of radiation, and hence cannot couple this momentum to the larger scale ISM. Thus, it would be incorrect to compute an effective $f_{\rm trap}$ and impart this momentum in unresolved simulations without considering the corresponding enhancement of gravity due to the presence of unresolved bound structures, as embodied by $f_{\rm grav}$. To be consistent, a model should either set both $f_{\rm trap}$ and $f_{\rm grav}$ to zero (i.e. no subgrid trapping), or include an explicit subgrid estimate of both, with the condition that, if $f_{\rm trap} < f_{\rm grav}$, no momentum is imparted to the gas on resolved scales because all of the radiation momentum is advected back into the stars.[10] The reason that some previous models have found IR radiation feedback to be effective is that likely they were not consistent, because they set $f_{\rm trap} > 1$, but implicitly adopted $f_{\rm grav} = 0$.

4.3.3 Comparison to observational estimates

In Fig. 19 we plot the time evolution of $f_{\rm trap, cl} \equiv f_{\rm trap}(r \to R_{\rm cloud})$, the cumulative momentum imparted through the entire cloud for

---

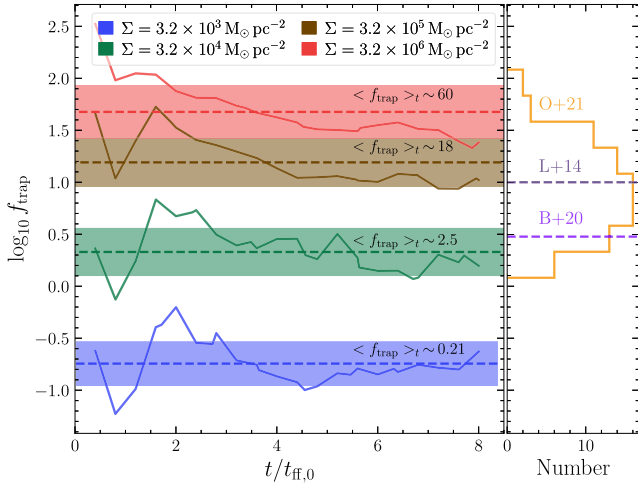[10]See Krumholz (2018) for a sub-grid model that attempts this in the single-scattering limit.

Figure 19. Comparison of the time evolution of the cumulative IR radiation trapping factor through the cloud ($f_{\rm trap, cl} \equiv f_{\rm trap}(r \rightarrow R_{\rm cloud})$) for the four values of $\Sigma_{\rm cloud}$. Dashed lines indicate the time-averaged value of $f_{\rm trap, cl}$ for each case, which is also annotated in the figure, and the shaded bands indicate the 1σ variations. The panel on the right shows observational estimates of $f_{\rm trap}$: (i) histogram of $f_{\rm trap}$ values derived for young, compact, H II regions in the W49A star-forming region from Olivier et al. (2021, O + 21) (ii) median value of $f_{\rm trap}$ inferred for H II regions in the Central Molecular Zone (CMZ) from Barnes et al. (2020, B + 20), and (iii) the median value of $f_{\rm trap}$ for H II regions in the Large and Small Magellanic clouds probed by Lopez et al. (2014, L + 14).

our runs; we denote the time-average of this quantity throughout a simulation as $\langle f_{\rm trap, cl} \rangle_t$. We see that $f_{\rm trap, cl}$ increases for higher $\Sigma_{\rm cloud}$ – consistent with the expectation of more trapping at higher surface densities – with $\langle f_{\rm trap, cl} \rangle_t \sim 0.2$ for the lowest $\Sigma_{\rm cloud}$, and $\langle f_{\rm trap, cl} \rangle_t \sim 60$ for the highest $\Sigma_{\rm cloud}$ case. We also see significant time evolution in this quantity, especially at higher $\Sigma_{\rm cloud}$, displaying signs of a decline at later times. This variation is driven by the corresponding time variations in $\tau_{\rm IR}$, which decreases as the cloud is depleted by accretion through the cloud; clouds maintain a fairly (temporally) constant ratio of $f_{\rm trap, cl}$ to $\tau_{\rm IR}$. We also compare our (time-averaged) estimates of $f_{\rm trap}$ with observational estimates for it in Fig. 19. We can see that the values of $f_{\rm trap}$ obtained in our simulations span similar ranges as observational estimates.

4.4 Implications for star formation in dense/starburst environments

The evolution of clouds in our simulations suggest that IR radiation pressure is unlikely to play a dynamically important role in regulating ϵ_* in extreme environments, which presumably are locations where SSCs would form. We find values of $\epsilon_* \sim 80$ per cent, in contrast to Milky Way-like GMCs, which reach integrated efficiencies of only $\epsilon_* \sim 5$–20 per cent (and references therein Chevance et al. 2022a). This is probably maintained in Milky Way GMCs through a combination of turbulence, magnetic fields, and dynamically competitive feedback mechanisms (e.g. Federrath 2015; Grudić et al. 2018). Our simulations show that IR radiation feedback cannot compete with gravity in this regime, and other feedback mechanisms are also expected to be ineffective in this regime of Σ (see the review by Krumholz et al. 2019). Turbulence driven by galactic-scale forces (e.g. tidal shear from a galactic collision – common in galaxies forming SSCs) may be able to slow down star formation,

and lead to lower integrated star formation efficiencies by dispersing unbound gas – as evidenced by simulations with initially unbound clouds ($\alpha_{\rm vir}$ series; Table 1). However, even in these cases, we find $\epsilon_* \gtrsim 60$ per cent. Our findings therefore suggest that star formation in dense environments such as proto-SSCs and nuclear star clusters should achieve high efficiencies (~ 60–80 per cent), and are therefore very likely to be gravitationally bound at formation.

This is consistent with recent observational studies of SSC and proto-SSC environments in the local Universe. Efficiencies of $\epsilon_* \sim 50$–80 per cent and high fractions of stars in bound clusters have been inferred for the dense star-forming regions in the starburst galaxies NGC 253 (Leroy et al. 2018; Rico-Villas et al. 2020), NGC 5253 (Turner et al. 2015), NGC 4945 (Emig et al. 2020), Arp 240 (He et al. 2020), Antennae (Finn et al. 2019; He et al. 2022), and Henize 2-10 (Costa et al. 2021). While high ratios of stellar to gas mass (which is ultimately what these observations measure) can be a sign of gas dispersal even when ϵ_* is low, line-widths of dense gas tracers, and an observed presence of quiescent dense gas within clusters (Turner et al. 2015; Rico-Villas et al. 2020), suggests this is unlikely to be the case.

The main exception to this trend is presented in Levy et al. (2021), who analyse high-resolution (~ 0.5 pc) observations of SSCs in NGC 253 and find that a subset of their sample shows signs of (dense gas) outflows indicated by P-Cygni profiles in the spectra of multiple tracers, with inferred mass fluxes large enough to substantially reduce ϵ_*. They suggest that radiation pressure and/or stellar winds are the most likely candidates to drive this outflow, but our work shows that the former is unlikely. The low efficiency of wind-driven feedback found in recent models (Lancaster et al. 2021a,b) suggests that winds are also unlikely to be the primary driver of these outflows. However, we note that the simulations in Lancaster et al. (2021b) are limited to environments with $\Sigma \lesssim 3.2 \times 10^3$ M$_\odot$ pc^{-2}; simulations of stellar wind feedback in more extreme environments – such as NGC 253 – have not been performed to our knowledge. It is also possible that the combined effects of stellar winds and radiation pressure are able to unbind gas, and drive outflows. Therefore, it remains an open question as to what drives these observed outflows; future observations of proto-SSCs to compile a statistical sample, coupled with models/simulations that incorporate multiple feedback mechanisms, are needed to address this question.

4.5 Caveats

We end this discussion by pointing out that our numerical simulations are missing several physical mechanisms that might play a further role in regulating star formation, and hence stress that the reader interpret our results in light of these limitations. We briefly discuss these caveats and speculate the effects they might have on our results.

The primary caveat is that we do not model the direct stellar UV radiation field in our simulations, thereby omitting two other feedback mechanisms: photoionization of hydrogen and the associated thermal pressure, and the single-scattering UV radiation pressure. The former would play a relatively minor role for the parameter space we are exploring: the escape speeds of even our lowest $\Sigma_{\rm cloud}$ run is ~ 30 km s^{-1}, significantly greater than the ionized gas sound speed (~ 10 km s^{-1}), a limit at which earlier studies have shown that ionizing feedback is dynamically subdominant to both radiation pressure and gravity (Dale et al. 2012; Kim et al. 2018). On the other hand, the UV radiation pressure on dust could be important as the dust opacity at these wavelengths can be 2–3 orders of magnitude higher than in the IR (e.g. Draine 2011), and the available momentum

would be imparted closer to the stars. Not directly including the UV systematically underestimates the forces of radiation in all our models by at most a value of $\sim L_*/c$. This might provide additional support against gravity that might be sufficient for radiation pressure to be dynamically relevant. However, in clouds with high f_{trap}, including the direct UV force would have a very modest effect, as it would change f_{Edd} by about $\sim 1/f_{\text{trap}}$ – insufficient to render the cloud super-Eddington. However, this need not be the case for the lower Σ_{cloud} cases, where f_{trap} is of the order of a few; here the direct UV can be comparable, or even dominant over the total radiation force, and is crucial to obtain the correct total radiation force. Single-scattering radiation pressure also has the attractive property that even if the cloud is globally sub-Eddington to this force, it can eject gas in sightlines that have lower Σ set by turbulence (Thompson & Krumholz 2016; Wibking et al. 2018). In other words, there is always the possibility that some fraction of the cloud be susceptible to being ejected by the direct UV radiation pressure. Combined with the IR radiation pressure, it is possible that the dynamical outcomes of some our model clouds be affected. We also note that, because we do not model the UV radiation field directly, we must rely on a spherically symmetric source term for IR photons (equation 15), which does not take into account the asymmetric density distribution of matter around the sources of radiation. This conceivably leads us to underestimate the effectiveness of IR radiation on very small scales, where direct radiation would deposit energy most efficiently in the densest structures. It is therefore of interest to model the radiation field in both the UV and IR bands, including the contribution of the direct UV radiation pressure along with the IR pressure, self-consistently injecting IR photons via the reprocessing of the absorbed UV photons by dust, and thereby accounting for non-symmetric density distributions.

We also do not include magnetic fields in our simulations. Magnetic fields have been shown to play a role in the effectiveness of feedback mechanisms – by coupling forces from impulsive, localized mechanisms such as protostellar outflows/jets to a more extended region (e.g. Nakamura & Li 2007; Wang et al. 2010; Federrath et al. 2014; Offner & Liu 2018), or minimizing energy losses due to mixing/conduction in energy-driven feedback mechanisms such as stellar winds or supernovae (e.g. Markevitch & Vikhlinin 2007; Gentry et al. 2019). However, we argue that these effects are unlikely to be important for the IR radiation pressure force, which is a more volume-filling, momentum-driven mechanism, for which magnetic fields do not directly alter the force that can be imparted. However, magnetic fields can provide additional support against gravitational collapse and therefore possibly render higher fractions of gas unbound (e.g. Krumholz & Federrath 2019), in analogy to the effects we find by raising α_{vir}, but with the advantage that magnetic support does not decay the way turbulent support does. We cannot entirely rule out the possibility that with this additional support, the radiation forces might become dynamically important. We also do not include explicit, continuous, turbulence driving, which emulates the turbulent cascade from larger scales in the ISM – this too might act as an additional source of support. Therefore, the reader should interpret our high values of ϵ_* with caution, as there are additional mechanisms that might work together in a non-trivial way to potentially enhance the role of radiation feedback.

5 CONCLUSIONS

We conduct 3D radiation hydrodynamic simulations of star cluster formation and evolution in massive, dusty, self-gravitating clouds in the multiple-scattering limit, with an aim to determine the star formation efficiency (ϵ_*) of clouds set by the competition between gravity and IR radiation pressure. We use the recently developed VETTAM algorithm (Menon et al. 2022), which uses the state-of-the-art Variable Eddington Tensor closure, and, unlike earlier radiative transfer methods, allows us to sample a broad range of cloud surface densities ($\Sigma_{\text{cloud}} \sim 10^3$–$10^6$ $M_\odot$ pc^{-2}). Thus, our simulations cover the range of conditions found in young massive clusters and superstar clusters, in both the Milky Way and denser starburst environments. We also compare the results using models for dust opacity at increasing levels of realism – constant opacities, a commonly used power-law approximation valid at low temperatures, and opacities taken from a more realistic, complex dust model (Semenov et al. 2003) – and using a range of dust-to-gas ratios. We draw the following conclusions from our simulations:

(i) For realistic dust opacities, infrared radiation pressure is highly unlikely to regulate star formation, even at the highest cloud surface densities. We find that the star formation efficiency $\epsilon_* \sim 80$ per cent in our simulations, and radiation pressure does not show any evidence of driving winds or inhibiting accretion. This occurs because the clouds are sub-Eddington at all radii.

(ii) This conclusion continues to hold even for clouds that are initially unbound, or that are dust-enriched up to twice the solar-neighbourhood dust-to-gas ratio. Only for dust-to-gas ratios of ~ 3 times solar does IR radiation feedback play some role, and even then it produces only a ~ 10 per cent reduction in ϵ_*.

(iii) Radiation forces are relatively weak due to a combination of modest IR dust opacities, and radiation-matter anticorrelation that renders feedback inefficient. We find that with realistic IR opacities, the former is primary, as it is sufficient by itself to render clouds wholly sub-Eddington; the latter just aggravates the ineffectiveness of feedback, and only becomes significant for supersolar dust-to-gas ratios ($\gtrsim 3 \times$ solar), or for radiation sources with significantly higher light-to-mass ratios than stellar populations with a standard IMF (e.g. individual massive stars).

(iv) These results depend critically on using realistic temperature-dependent dust opacities. Both of the approximations we test – using constant IR opacities sampled at the peak of the Semenov et al. (2003) opacity curve (~ 10 cm^2 g^{-1}) or using a pure power-law scaling for the opacity as a function of temperature – overestimate the opacity and thus the effects of radiation. The constant-opacity approximation fails because only very small localized regions of the cloud are at these opacities, and the power-law approximation fails because it leads to opacities that are far too large in the warmer parts of clouds (at temperatures $\gtrsim 100$ K). The fact that these approximations yield qualitatively different conclusions than our simulations with more realistic opacities calls into question a number of results in the literature that are based on them (in particular the role of radiation in limiting ϵ_* and in driving large-scale galactic winds).

(v) Despite the ineffectiveness of IR radiation feedback, IR radiation can none the less be effectively trapped and impart significantly more momentum to dusty gas than would be the case in the single-scattering limit; trapping factors in our simulations span the range $f_{\text{trap}} \sim 0.2$–60, depending on the cloud surface density, and those simulations with surface densities comparable to those seen around the Milky Way H II regions produce trapping factors in reasonable agreement with observationally inferred values. However, this momentum does not couple to the larger scale ISM, because the gas that receives this momentum is eventually accreted, i.e. we show that under the conditions where $f_{\text{trap}} > 1$, gravity dominates radiation. Subgrid models that include IR radiation feedback with $f_{\text{trap}} > 1$, but do not include the effects of gravity at unresolved scales and its effects on confining the gas, are therefore inconsistent.

Since IR radiation pressure is thought to be the only significant feedback mechanism at very high surface density, our results imply that regions such as (proto-) super star clusters (SSCs) in starburst environments (e.g. Leroy et al. 2018), or other extreme stellar systems in our Universe such as nuclear star clusters, should form stars very efficiently and with a large fraction of the stars confined to bound structures. Only if another physical feedback mechanism that is unaccounted for in our simulations or a non-trivial combination of physical effects (such as magnetic fields, turbulence and jet/outflow feedback) becomes important, would this picture change. There is significant scope to study star formation in such extreme environments with more sophisticated numerical simulations, and statistically significant sample sizes of observed SSC-forming regions.

ACKNOWLEDGEMENTS

DATA AVAILABILITY

Outputs of our simulations would be shared on reasonable request to the corresponding author.

REFERENCES

Adamo A. et al., 2020, Space Sci. Rev., 216, 69
Balay S., Gropp W. D., McInnes L. C., Smith B. F., 1997, in Arge E., Bruaset A. M., Langtangen H. P., eds, Modern Software Tools in Scientific Computing. Birkhäuser Press, Basel, p. 163
Balay S. et al., 2021, Technical Report ANL-21/39 - Revision 3.16, PETSc/TAO users Manual. Argonne National Laboratory, Lemont, IL
Barcos-Muñoz L. et al., 2017, ApJ, 843, 117
Barnes A. T., Longmore S. N., Dale J. E., Krumholz M. R., Kruijssen J. M. D., Bigiel F., 2020, MNRAS, 498, 4906
Bate M. R., Keto E. R., 2015, MNRAS, 449, 2643
Berger M. J., Colella P., 1989, J. Comput. Phys., 82, 64
Bieri R., Dubois Y., Rosdahl J., Wagner A., Silk J., Mamon G. A., 2017, MNRAS, 464, 1854
Buntemeyer L., Banerjee R., Peters T., Klassen M., Pudritz R. E., 2016, New Astron., 43, 49
Burkhart B., 2018, ApJ, 863, 118
Calura F., Few C. G., Romano D., D'Ercole A., 2015, ApJ, 814, L14
Castor J. I., 2004, Radiation Hydrodynamics. Cambridge Univ. Press, Cambridge
Castor J., McCray R., Weaver R., 1975, ApJ, 200, L107
Chevance M. et al., 2020, Space Sci. Rev., 216, 50
Chevance M., Krumholz M. R., McLeod A. F., Ostriker E. C., Rosolowsky E. W., Sternberg A., 2022a, preprint (arXiv:2203.09570)
Chevance M. et al., 2022b, MNRAS, 509, 272
Costa T., Rosdahl J., Sijacki D., Haehnelt M. G., 2018, MNRAS, 479, 2079
Costa A. H., Johnson K. E., Indebetouw R., Finn M. K., Brogan C. L., Reines A., 2021, ApJ, 918, 76
Crocker R. M., Krumholz M. R., Thompson T. A., Baumgardt H., Mackey D., 2018, MNRAS, 481, 4895
Curti M., Mannucci F., Cresci G., Maiolino R., 2020, MNRAS, 491, 944
Dale J. E., Ercolano B., Bonnell I. A., 2012, MNRAS, 424, 377
Davis S. W., Jiang Y.-F., Stone J. M., Murray N., 2014, ApJ, 796, 107
Draine B. T., 2011, ApJ, 732, 100
Dubey A., Reid L. B., Fisher R., 2008, Phys. Scr. T, 132, 014046
Elmegreen B. G., 2009, in Andersen J., Bland-Hawthorn J., Nordström B., eds, Proc. IAU Symp. 254, The Galaxy Disk in Cosmological Context. Cambridge Univ. Press, Cambridge, p. 289
Emig K. L. et al., 2020, ApJ, 903, 50
Evans N. J. II, Heiderman A., Vutisalchavakul N., 2014, ApJ, 782, 114
Evans N. J., Kim J.-G., Ostriker E. C., 2022, ApJ, 929, L18
Fall S. M., Krumholz M. R., Matzner C. D., 2010, ApJ, 710, L142
Federrath C., 2013a, MNRAS, 436, 1245
Federrath C., 2013b, MNRAS, 436, 3167
Federrath C., 2015, MNRAS, 450, 4035
Federrath C., Klessen R. S., 2012, ApJ, 761, 156
Federrath C., Klessen R. S., Schmidt W., 2008, ApJ, 688, L79
Federrath C., Roman-Duval J., Klessen R. S., Schmidt W., Mac Low M. M., 2010, A&A, 512, A81
Federrath C., Banerjee R., Clark P. C., Klessen R. S., 2010c, ApJ, 713, 269
Federrath C., Banerjee R., Seifried D., Clark P. C., Klessen R. S., 2011a, in Alves J., Elmegreen B. G., Girart J. M., Trimble V., eds, Proc. IAU Symp. 270, Computational Star Formation. Cambridge Univ. Press, Cambridge, p. 425
Federrath C., Sur S., Schleicher D. R. G., Banerjee R., Klessen R. S., 2011b, ApJ, 731, 62
Federrath C., Schrön M., Banerjee R., Klessen R. S., 2014, ApJ, 790, 128
Federrath C., Klessen R. S., Iapichino L., Beattie J. R., 2021, Nat. Astron., 5, 365
Federrath C., Roman-Duval J., Klessen R. S., Schmidt W., Mac Low M. M., 2022, TG: Turbulence Generator, Astrophysics Source Code Library, record ascl:2204.001
Finn M. K., Johnson K. E., Brogan C. L., Wilson C. D., Indebetouw R., Harris W. E., Kamenetzky J., Bemis A., 2019, ApJ, 874, 120
Fryxell B. et al., 2000, ApJS, 131, 273
Fukushima H., Yajima H., 2021, MNRAS, 506, 5512
Gallegos-Garcia M., Burkhart B., Rosen A. L., Naiman J. P., Ramirez-Ruiz E., 2020, ApJ, 899, L30
Gavagnin E., Bleuler A., Rosdahl J., Teyssier R., 2017, MNRAS, 472, 4155
Geen S., Hennebelle P., Tremblin P., Rosdahl J., 2016, MNRAS, 463, 3129
Gentry E. S., Krumholz M. R., Madau P., Lupi A., 2019, MNRAS, 483, 3647
Grasha K. et al., 2019, MNRAS, 483, 4707
Gritschneder M., Naab T., Walch S., Burkert A., Heitsch F., 2009, ApJ, 694, L26
Grudić M. Y., Hopkins P. F., Faucher-Giguère C.-A., Quataert E., Murray N., Kereš D., 2018, MNRAS, 475, 3511
Grudić M. Y., Guszejnov D., Offner S. S. R., Rosen A. L., Raju A. N., Faucher-Giguère C.-A., Hopkins P. F., 2022, MNRAS, 512, 216

Harris C. R. et al., 2020, Nature, 585, 357

He H., Wilson C. D., Sliwa K., Iono D., Saito T., 2020, MNRAS, 496, 5243

He H., Wilson C., Brunetti N., Finn M., Bemis A., Johnson K., 2022, ApJ, 928, 57

Heyer M., Gutermuth R., Urquhart J. S., Csengeri T., Wienen M., Leurini S., Menten K., Wyrowski F., 2016, A&A, 588, A29

Hollyhead K., Bastian N., Adamo A., Silva-Villa E., Dale J., Ryon J. E., Gazak Z., 2015, MNRAS, 449, 1106

Hopkins A. M., 2018, Publ. Astron. Soc. Aust., 35, e039

Hopkins P. F., Murray N., Quataert E., Thompson T. A., 2010, MNRAS, 401, L19

Hopkins P. F., Quataert E., Murray N., 2011, MNRAS, 417, 950

Hopkins P. F., Quataert E., Murray N., 2012, MNRAS, 421, 3522

Hu Z., Krumholz M. R., Pokhrel R., Gutermuth R. A., 2022, MNRAS, 511, 1431

Hunter J. D., 2007, Comput. Sci. Eng., 9, 90

Jacquet E., Krumholz M. R., 2011, ApJ, 730, 116

Jiang Y.-F., 2021, ApJS, 253, 49

Jiang Y.-F., Davis S. W., Stone J. M., 2013, ApJ, 763, 102

Kim C.-G., Ostriker E. C., 2017, ApJ, 846, 133

Kim J.-G., Kim W.-T., Ostriker E. C., Skinner M. A., 2017, ApJ, 851, 93

Kim J.-G., Kim W.-T., Ostriker E. C., 2018, ApJ, 859, 68

Krumholz M. R., 2018, MNRAS, 480, 3468

Krumholz M. R., Federrath C., 2019, Front. Astron. Space Sci., 6, 7

Krumholz M. R., Matzner C. D., 2009, ApJ, 703, 1352

Krumholz M. R., McKee C. F., 2005, ApJ, 630, 250

Krumholz M. R., Tan J. C., 2007, ApJ, 654, 304

Krumholz M. R., Thompson T. A., 2012, ApJ, 760, 155

Krumholz M. R., Thompson T. A., 2013, MNRAS, 434, 2329

Krumholz M. R., Matzner C. D., McKee C. F., 2006, ApJ, 653, 361

Krumholz M. R., Klein R. I., McKee C. F., Bolstad J., 2007, ApJ, 667, 626

Krumholz M. R., Klein R. I., McKee C. F., Offner S. S. R., Cunningham A. J., 2009, Science, 323, 754

Krumholz M. R., Dekel A., McKee C. F., 2012a, ApJ, 745, 69

Krumholz M. R., Klein R. I., McKee C. F., 2012b, ApJ, 754, 71

Krumholz M. R. et al., 2014, in Beuther H., Klessen R. S., Dullemond C. P., Henning T., eds, Protostars and Planets VI. University of Arizona Press, Tucson, p. 243

Krumholz M. R., McKee C. F., Bland-Hawthorn J., 2019, ARA&A, 57, 227

Kuiper R., Klahr H., Beuther H., Henning T., 2012, A&A, 537, A122

Lancaster L., Ostriker E. C., Kim J.-G., Kim C.-G., 2021a, ApJ, 914, 89

Lancaster L., Ostriker E. C., Kim J.-G., Kim C.-G., 2021b, ApJ, 922, L3

Lane H. B., Grudić M. Y., Guszejnov D., Offner S. S. R., Faucher-Giguère C.-A., Rosen A. L., 2022, MNRAS, 510, 4767

Leroy A. K. et al., 2017, ApJ, 846, 71

Leroy A. K. et al., 2018, ApJ, 869, 126

Levy R. C. et al., 2021, ApJ, 912, 4

Lopez L. A., Krumholz M. R., Bolatto A. D., Prochaska J. X., Ramirez-Ruiz E., 2011, ApJ, 731, 91

Lopez L. A., Krumholz M. R., Bolatto A. D., Prochaska J. X., Ramirez-Ruiz E., Castro D., 2014, ApJ, 795, 121

Mac Low M.-M., Klessen R. S., 2004, Rev. Mod. Phys., 76, 125

MacNeice P., Olson K. M., Mobarry C., de Fainchtein R., Packer C., 2000, Comput. Phys. Commun., 126, 330

Markevitch M., Vikhlinin A., 2007, Phys. Rep., 443, 1

Marshak R. E., 1958, Phys. Fluids, 1, 24

McCrady N., Graham J. R., Vacca W. D., 2005, ApJ, 621, 278

Meidt S. E. et al., 2018, ApJ, 854, 100

Menon S. H., Federrath C., Kuiper R., 2020, MNRAS, 493, 4643

Menon S. H., Federrath C., Klaassen P., Kuiper R., Reiter M., 2021, MNRAS, 500, 1721

Menon S. H., Federrath C., Krumholz M. R., Kuiper R., Wibking B. D., Jung M., 2022, MNRAS, 512, 401

Mihalas D., Auer L., 2001, J. Quant. Spectrosc. Radiat. Transfer, 71, 61

Mihalas D., Klein R. I., 1982, J. Comput. Phys., 46, 97

Murray N., Quataert E., Thompson T. A., 2010, ApJ, 709, 191

Nakamura F., Li Z.-Y., 2007, ApJ, 662, 395

Offner S. S. R., Liu Y., 2018, Nat. Astron., 2, 896

Olivier G. M., Lopez L. A., Rosen A. L., Nayak O., Reiter M., Krumholz M. R., Bolatto A. D., 2021, ApJ, 908, 68

Ostriker E. C., McKee C. F., Leroy A. K., 2010, ApJ, 721, 975

Padoan P., Federrath C., Chabrier G., Evans N. J. II, Johnstone D., Jørgensen J. K., McKee C. F., Nordlund Å., 2014, Protostars and Planets VI. University of Arizona Press, Tucson

Padoan P., Pan L., Haugbølle T., Nordlund Å., 2016, ApJ, 822, 11

Park H., Knoll D. A., Rauenzahn R. M., Wollaber A. B., Densmore J. D., 2012, Transp. Theory Stat. Phys., 41, 284

Pokhrel R. et al., 2020, ApJ, 896, 60

Portegies Zwart S., McMillan S., Gieles M., 2010, ARA&A, 48, 431

Raskutti S., Ostriker E. C., Skinner M. A., 2016, ApJ, 829, 130

Reissl S., Klessen R. S., Low M. M. M., Pellegrini E. W., 2018, A&A, 611, A70

Ricker P. M., 2008, ApJS, 176, 293

Rico-Villas F., Martín-Pintado J., González-Alfonso E., Martín S., Rivilla V. M., 2020, MNRAS, 491, 4573

Rogers H., Pittard J. M., 2013, MNRAS, 431, 1337

Rosdahl J., Teyssier R., 2015, MNRAS, 449, 4380

Rosen A. L., Lopez L. A., Krumholz M. R., Ramirez-Ruiz E., 2014, MNRAS, 442, 2701

Rosen A. L., Krumholz M. R., McKee C. F., Klein R. I., 2016, MNRAS, 463, 2553

Saad Y., 2003, Iterative Methods for Sparse Linear Systems: Second Edition, Other Titles in Applied Mathematics. Society for Industrial and Applied Mathematics, Philadelphia, available at: https://books.google.com.au/books?id = qtzmkzzqFmcC

Semenov D., Henning T., Helling C., Ilgner M., Sedlmayr E., 2003, A&A, 410, 611

Skinner M. A., Ostriker E. C., 2013, ApJS, 206, 21

Skinner M. A., Ostriker E. C., 2015, ApJ, 809, 187

Smith L. J., Bajaj V., Ryon J., Sabbi E., 2020, ApJ, 896, 84

Thompson T. A., Krumholz M. R., 2016, MNRAS, 455, 334

Thompson T. A., Quataert E., Murray N., 2005, ApJ, 630, 167

Truelove J. K., Klein R. I., McKee C. F., Holliman, John H. I., Howell L. H., Greenough J. A., 1997, ApJ, 489, L179

Tsang B. T. H., Milosavljević M., 2015, MNRAS, 453, 1108

Tsang B. T. H., Milosavljević M., 2018, MNRAS, 478, 4142

Turk M. J., Smith B. D., Oishi J. S., Skory S., Skillman S. W., Abel T., Norman M. L., 2010, ApJS, 192, 9

Turner J. L., Beck S. C., Benford D. J., Consiglio S. M., Ho P. T. P., Kovács A., Meier D. S., Zhao J. H., 2015, Nature, 519, 331

Turner J. L., Consiglio S. M., Beck S. C., Goss W. M., Ho P. T. P., Meier D. S., Silich S., Zhao J.-H., 2017, ApJ, 846, 73

Utomo D. et al., 2018, ApJ, 861, L18

Virtanen P. et al., 2020, Nat. Methods, 17, 261

Waagan K., Federrath C., Klingenberg C., 2011, J. Comput. Phys., 230, 3331

Wang P., Li Z., Abel T., Nakamura F., 2010, ApJ, 709, 27

Weaver R., McCray R., Castor J., Shapiro P., Moore R., 1977, ApJ, 218, 377

Wibking B. D., Thompson T. A., Krumholz M. R., 2018, MNRAS, 477, 4665

Zhang D., 2018, Galaxies, 6, 114

Zhang D., Davis S. W., 2017, ApJ, 839, 54

Zhang D., Davis S. W., Jiang Y.-F., Stone J. M., 2018, ApJ, 854, 110

APPENDIX A: NUMERICAL CONVERGENCE STUDIES

In this section, we test the dependencies of our results on certain numerical choices that have been made in our simulations. Since the fiducial simulations are all sub-Eddington, the values of ϵ_* attained are virtually identical, irrespective of these numerical choices. Therefore, we found it more informative to compare the Eddington ratio $f_{\rm Edd}$ with different numerical choices.
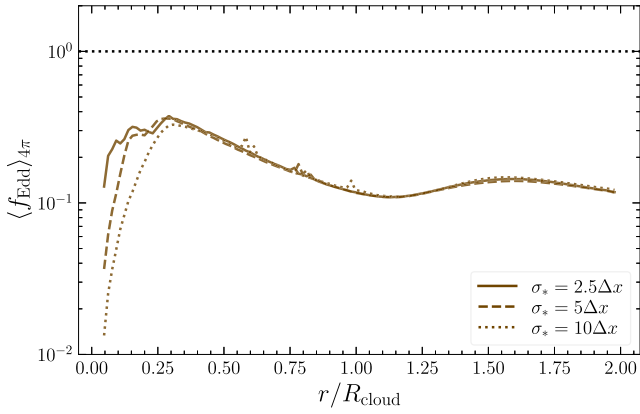
Figure A1. Comparison of the obtained Eddington ratios for the run S5KSemA2F1 at $t = 3\,t_{\rm ff}$, with different choices for the source size (σ_*). The choice adopted in our study is $\sigma_* = 2.5\Delta x$, where Δx is the cell width.
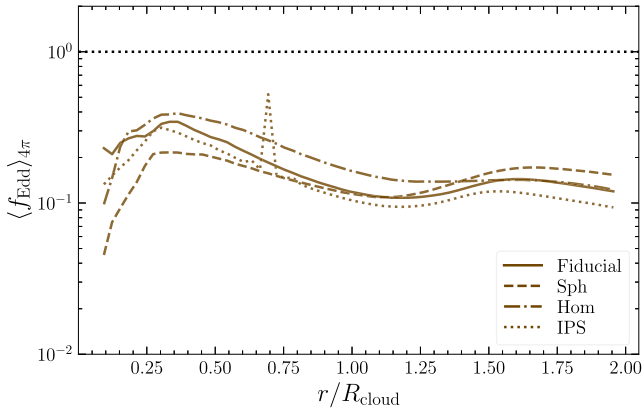

Figure A2. Eddington ratios at $t = 3\,t_{\rm ff}$ in run S5KSemA2F1 repeated using different micro-physical properties. The opacities in the fiducial run assume that dust grains are aggregate particles made of composite materials with normal iron content in the silicates. The alternative models shown use spherical (Sph) rather than aggregate particles, homogeneous (Hom) rather than composite dust, and iron-poor silicates (IPS) rather than normal iron content. See the text for further details.
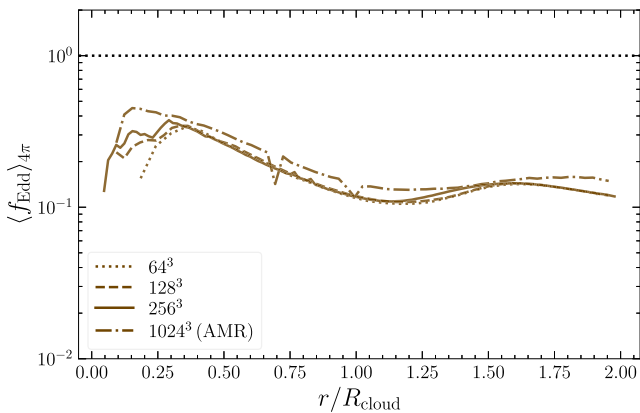

Figure A3. Comparison of the obtained Eddington ratios for the fiducial run at $t = 3\,t_{\rm ff}$, with different grid resolutions. The solid lines indicate the resolution used in exploring parameter space in our study. The AMR run had an effective maximum resolution of 1024^3 cells. We see that the runs are reasonably converged with resolution.

A1 Dependence on source size

Here we test the dependence of our results on the adopted choice for the size of the source σ_* in equation (15). Our fiducial choice is $\sigma_* = 2.5\Delta x$, where Δx is the size of a computational cell on the highest level of AMR where the sink particle is located; for our fiducial resolution, this corresponds to $\sigma_* = 0.039\,R_{\rm cloud}$. We check the dependence of our results on this choice by repeating run S5KSemA2F1 with alternate choices of $\sigma_* = 5\Delta x = 0.078\,R_{\rm cloud}$ and $\sigma_* = 10\Delta x = 0.16\,R_{\rm cloud}$. We plot the Eddington ratios we obtain at $t = 3\,t_{\rm ff}$ for this test in Fig. A1. We see that all the curves are nearly identical at all radii substantially larger than σ_*; at $r \lesssim \sigma_*$, the Eddington ratio $f_{\rm Edd}$ decreases because j_* is smoothed in this region, and hence radiation forces are smaller. Based on this test we conclude that the effects of smoothing are minimal for our fiducial choice of σ_*, because Fig. A1 demonstrates that smoothing has negligible effects outside the smoothed volume, and the volume that is affected for $\sigma_* = 2.5\Delta x$ is only $\sim 10^{-5}$ of the total cloud volume.

A2 Dependence on the microphysical dust model

Since we find that realistic dust opacities (i.e. $\kappa_{\rm Sem}$) are crucial to our results, it is important to check for any dependencies on the particulars of the dust model. Semenov et al. (2003) present a range of possible models, based on differing assumptions regarding the microphysical nature of dust grains – specifically their topology, shape, and chemical composition. Our default choices are grains with an 'aggregate' shape (i.e. they are a cluster of small spherical sub-grains sticking together), composite' composition (i.e. they incorporate a mixture of materials), and 'normal' (NRM) iron content in the dust silicates; alternative assumptions for each of these properties lead to changes in the opacity (see fig. 1 in Semenov et al. 2003).

To test the sensitivity of our results to these choices, we again repeat run S5KSemA2F1 using some of Semenov et al.'s alternative dust models. We test the following choices: 'spherical' particles instead of a cluster of subgrains, 'homogeneous' rather than heterogeneous composition, and 'Iron-poor silicates' (IPS) instead of normal (NRM) iron content; for each of these variations, we leave the remaining properties unchanged, e.g. our spherical grain models have composite composition and normal iron content. We plot the Eddington ratios $f_{\rm Edd}$ obtained from these experiments in Fig. A2. We see that alternative dust models lead to mild changes in the Eddington ratio, but the results are qualitatively quite similar (the same to within a factor of $\lesssim 2$), and most importantly, all are sub-Eddington. This suggests that our major results are robust against plausible changes in the assumed micro-physical dust properties.

A3 Dependence on resolution

We test for numerical convergence of our results by comparing runs with different grid resolutions. We again repeat simulation S5KSemA2F1 with uniform-grid resolutions of 64^3 and 128^3 to compare with our fiducial choice of 256^3, and we further compare to an AMR run with a base-grid resolution of 128^3, and 3 levels of refinement, thereby leading to a maximum effective resolution of 1024^3. For the AMR run we refine based on the Jeans length, requiring that it be resolved by at least 8 cells (Truelove et al. 1997; Federrath et al. 2011b). We compare the radial profiles of Eddington ratios in these runs in Fig. A3. We see that at higher resolution, the radial location of maximum $f_{\rm Edd}$ shifts inwards with increasing resolution. However, the maximum value of $f_{\rm Edd}$ shows

changes of at most ∼ 20 per cent, and over the bulk of the cloud, $f_{\rm Edd}$ is fairly independent of resolution. Therefore, we conclude that our qualitative results are insensitive to resolution, and thereby are reasonably converged.

APPENDIX B: IDEALIZED SPHERICALLY-SYMMETRIC MODEL CLOUD

Here we fully describe the semi-analytical model that we use to obtain the steady-state radial profiles of matter and radiation quantities in spherical symmetry. Our approach follows the one described in section 4.3.6 of Skinner & Ostriker (2013), modified to accommodate non-constant opacities. We model a spherically symmetric cloud of gas and stars with a total mass $M = 10^6$ M$_\odot$; the stars are located at the origin ($r = 0$), and we inject (IR) photons with a radial distribution that follows equation (15). Their luminosity $L_* = \langle L_*/M_* \rangle M_*$, where $M_* = \epsilon_* M$ is the stellar mass, ϵ_* is the mass fraction in stars, and $\langle L_*/M_* \rangle = 1.7 \times 10^3$ erg s^{-1} g^{-1}. We set the size of the source $\sigma_* = 0.03\, R_{\rm g}$, where $R_{\rm g}$ is the maximum radius of the cloud, but, as discussed in Appendix A1, this choice makes little difference at radii $r > \sigma_*$. We parametrize our model in terms of the gas mass surface density $\Sigma = M_{\rm g}/(\pi R_{\rm g}^2)$, and an index α such that $\rho \propto r^{-\alpha}$ describing the radial profile of gas density. For a given Σ and α, it is straightforward to obtain the normalization of the density profile required to reach the desired mass M. We set $\rho(r) = 10^{-10}\rho_0$ for $r > R_{\rm g}$, where $\rho_0 = M_{\rm g}/(4/3\pi R_{\rm g}^3)$, to emulate an optically thin background outside the cloud.

Given the parameters, the radial radiation flux F can then be obtained by solving the steady-state equation of E_r (equation 5),

$$\nabla \cdot F = j_*(r). \tag{B1}$$

This gives

$$F_*(r) = \frac{L_*}{4\pi r^2} \left[{\rm erf}\left(\frac{r}{\sqrt{2}\sigma_*}\right) - \frac{2r}{\sqrt{2\pi\sigma_*^2}} \exp\left(-\frac{r^2}{2\sigma_*^2}\right) \right]. \tag{B2}$$

The equation for the radiation momentum (equation 6) in steady state satisfies, in spherical coordinates,

$$\nabla \cdot \mathbf{P} = -\rho\kappa_{\rm R}\frac{\mathbf{F}}{c}, \tag{B3}$$

where $\mathbf{F}$ is the vector flux. Solving this equation for the radiation energy density E_r requires a closure relation. We use the analytical M_1 closure in this model, since it is both purely local (removing the need for any iteration) and exact for a single source. This closure expresses P_{rr}, the radial component of $\mathbf{P}$, in terms of E_r as $P_{rr} = f_{rr}E_r$, where f_{rr} is the radial-diagonal component of the Eddington tensor. Under the M_1 approximation, this is related to the reduced flux $\zeta = F/(cE_r)$ as

$$\zeta = \frac{5 - 2\sqrt{4 - 3f_{rr}^2}}{3}. \tag{B4}$$

The non-radial components of $\mathbf{P}$ that arise when applying the divergence operator can be written in terms of P_{rr} and E_r by using the fact that the trace of $\mathbf{P}$ is equal to E_r. Subsequent substitutions allow us to write an ODE for ζ given by

$$\partial_r\zeta = \frac{3\zeta\sqrt{4 - 3\zeta^2}}{5\sqrt{4 - 3\zeta^2} - 8} \left[\frac{\partial_r \ln F}{3}\left(5 - 2\sqrt{4 - 3\zeta^2}\right) \right.$$
$$\left. + \frac{2}{r}\left(2 - \sqrt{4 - 3\zeta^2}\right) + \rho\kappa_{\rm R}\zeta \right]. \tag{B5}$$
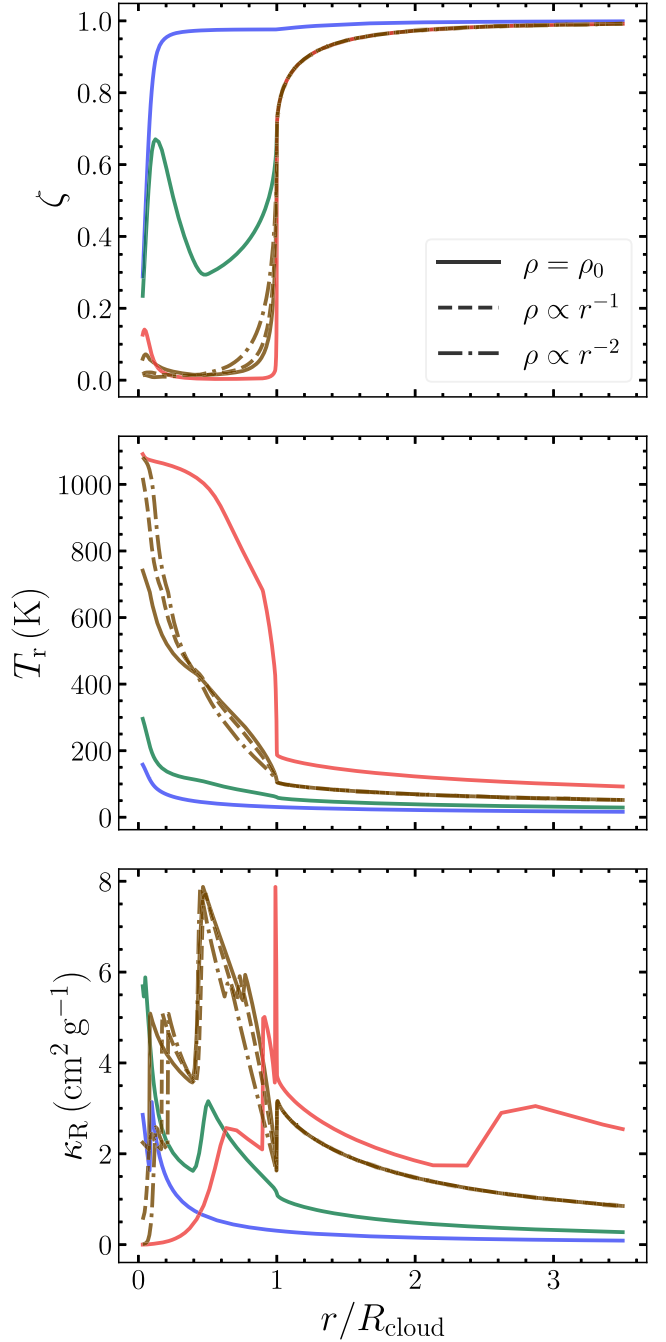
Figure B1. The reduced flux (ζ; top), radiation temperature ($T_{\rm r}$; middle), and Rosseland opacity ($\kappa_{\rm R}$; bottom) profiles obtained with the steady-state semi-analytic models described in Section B. Colours indicate the four values of $\Sigma_{\rm cloud}$ probed in our study; solid, dashed, and dash-dotted lines indicate values of α in the density profile.

This ODE passes through a critical point when $\zeta_{\rm crit} = 2\sqrt{3}/5$, at a radial location $r_{\rm crit}$ that can be obtained numerically by solving

$$3\partial_r \ln F + \frac{4}{r} + 2\sqrt{3}\rho\kappa_{\rm R} = 0. \tag{B6}$$

Our numerical procedure is to solve for the location of the critical point, and then integrate outwards and inwards in radius.

Thus far our approach parallels that of Skinner & Ostriker (2013). Where we diverge is that they treat the opacity $\kappa_{\rm R}$ as constant,

whereas for us the opacity is dependent on the radiation temperature $T_r = (E_r/a_R)^{0.25}$, which itself can be rewritten in terms of ζ (and F). This renders equation (B5) an ODE in one variable (ζ), which can be integrated numerically to obtain $\zeta(r)$, and subsequently $T_r(r)$, and $\kappa_R(r)$. We show the resulting profiles for some examples of Σ_{cloud} and α in Fig. B1.

Once we have obtained the profiles, it is straightforward to compute the radiative force as $f_{\mathrm{rad}} = \rho \kappa_R F/c$. The corresponding forces of gravity on the gas are given by the sum of their interaction with the source (g_*) and self-gravitational interactions (g_{self}) as

$f_{\mathrm{grav}} = \rho(g_{\mathrm{sink}} + g_{\mathrm{self}})$. The former is simply $g_* = GM_*/r^2$, and $g_{\mathrm{self}} = G \int_0^r \mathrm{d}M(r')/r^2$, where $\int_0^r \mathrm{d}M(r') = \int_0^r \rho(r')4\pi r'^2 \mathrm{d}r'$ is the cumulative gas mass out to radius r. These can then be combined to construct the Eddington ratio $f_{\mathrm{Edd}} = f_{\mathrm{rad}}/f_{\mathrm{grav}}$. The numerical implementation for this model is available at the following github repository: https://github.com/shm-1996/ModelCloud.

This paper has been typeset from a TEX/LATEX file prepared by the author.